Thesis for the Degree of Doctor of Philosophy

Beyond Breakaway Corrosion

Investigating the Secondary Corrosion Protection of Iron-based alloys

AMANDA PERSDOTTER

Department of Chemistry and Chemical Engineering
Chalmers University of Technology
Gothenburg, Sweden 2023

Beyond Breakaway Corrosion: Investigating the secondary corrosion protection of Iron-based alloys
Amanda Persdotter
ISBN 978-91-7905-943-9

Doktorsavhandlingar vid Chalmers tekniska högskola
Ny serie nr 5409
ISSN 0346-718X

Department of Chemistry and Chemical Engineering
Chalmers University of Technology
SE-412 96 Gothenburg, Sweden
Telephone +46 (0)31-772 1000

Cover: Schematic illustration of the oxidation kinetics for the primary corrosion protection (Cr/Al-rich M_2O_3), and secondary corrosion protection (multi-layered Fe-rich oxide) of Fe-based alloys at intermediate temperatures.

Chalmers Digitaltryck,
Gothenburg, Sweden 2023

Beyond Breakaway Corrosion: Investigating the Secondary corrosion protection of Iron-based alloys

AMANDA PERSDOTTER,
Department of Chemistry and Chemical Engineering
Chalmers University of Technology

Abstract

High temperature corrosion of metallic materials remains a major challenge for many industrial applications. The challenges of high temperature corrosion are often addressed by using highly alloyed materials such as stainless steels or FeCrAl alloys. The corrosion protection of these alloys rely on the formation of a protective Cr- and/or Al-rich corundum-type oxide. However, under corrosive conditions, these oxides tend to break down, resulting in the formation of a less protective, multi-layered Fe-rich oxide scale, a process known as *breakaway corrosion*.

The oxide scales formed after breakaway are often considered to be non-protective. Therefore, previous studies on breakaway corrosion have mainly focused on how to delay, or prevent, the breakdown of the Cr/Al-rich oxide. Nevertheless, in many industrial applications the breakaway event occurs in an early stage of operation and may be difficult to prevent. Thus, the corrosion propagation and lifetime of metallic components are often determined by the protection of the Fe-rich oxide scale formed after breakaway.

This thesis systematically investigates the protective properties of the Fe-rich oxides formed after breakaway at intermediate temperatures (400-600 °C). This is done through well-controlled breakdown of the Cr/Al-rich oxide, on a broad range of Fe-based model alloys that contain varying amounts of Cr, Ni, Al, and Si. The formed multi-layered Fe-rich oxide scales are subjected to detailed microstructural investigations, to elucidate how the properties and microstructures of the multi-layered Fe-rich oxide change as a result of altered alloy composition, and/or the presence of certain corrosive species.

The results clearly demonstrate the possibilities to improve the protection of the Fe-rich oxide by an altered alloy composition. The influences that alloying elements exhibit on the Fe-rich oxide scales are different from the previously demonstrated effects of the slow-growing Cr/Al-rich corundum-type oxides. Thus, the positive effects of certain alloying elements in Fe-based alloys are not necessarily the same for the corrosion protection exhibited before and after breakaway. Therefore, this thesis introduces the concept of primary and secondary corrosion protection for the oxide scales formed before (Cr/Al-rich corundum-type oxides) and after (multi-layered Fe-rich oxide scales) breakaway. The terminology is considered to be important for future material research and development, as well as for the selection of materials to be used in applications in which breakaway corrosion cannot be prevented.

Keywords: High temperature corrosion, Breakaway oxidation, Fe-based alloys, Iron oxide, Secondary corrosion protection

List of publications

This thesis is based on the following papers:

Paper I:
A. Persdotter, J. Eklund, J. Liske, T. Jonsson, Beyond breakaway corrosion - Influence of chromium, nickel and aluminum on corrosion of iron-based alloys at 600 °C, *Corrosion Science* 177:108961, 2020.

Paper II:
J. Eklund, **A. Persdotter**, I. Hanif, S. Bigdeli, T. Jonsson, Secondary corrosion protection of FeCr(Al) model alloys at 600 °C - The influence of Cr and Al after breakaway corrosion, *Corrosion Science* 189:109584, 2021.

Paper III:
A. Persdotter, H. Larsson, J. Eklund, S. Bigdeli, T. Jonsson, The influence of Nickel on the corrosion protection of FeCrNi alloys after breakaway corrosion at 600 °C, *In manuscript.*

Paper IV:
J. Eklund, **A. Persdotter**, V. Ssenteza, T. Jonsson, The long-term corrosion behavior of FeCrAl(Si) alloys after breakaway oxidation at 600 °C, *Corrosion Science* 217:111155, 2023.

Paper V:
A. Persdotter, T. Boll, V. Ssenteza, T. Jonsson, Insight into the influence of alloying elements on the secondary corrosion protection of Fe-based alloys by means of Atom probe tomography. *In manuscript.*

Paper VI:
A. Persdotter, M. Sattari, E. Larsson, M. A. Olivas Ogaz, J. Liske, T. Jonsson, Oxidation of Fe-2.25Cr-1Mo in presence of KCl(s) at 400 °C - Crack formation and its influence on oxidation kinetics, *Corrosion Science* 163:108234, 2020.

Paper VII:
A. Persdotter, T. Boll, T. Jonsson, Minor element effect on high temperature corrosion of a low-alloyed steel: Insight into alkali- and chlorine induced corrosion by means of atom probe tomography, *Corrosion Science* 192:109779, 2021.

Contribution report:

Paper I: I was the principal author, and had the main responsibility for planning of experimental work, SEM/EDX and FIB operation, data evaluation, conceptualisation and writing.

Paper II: I co-authored the paper, and had the main responsibility for the TEM analysis (part of TEM operation was performed by Dr. Imran Hanif) and data evaluation, as well as major part in conceptualisation and writing.

Paper III: I was the principal author, and the main person responsible for planning of experimental work, SEM/EDX analysis, data evaluation, conceptualisation, and writing.

Paper IV: I co-authored the paper and was the main responsible for the TEM analysis and data evaluation, as well as major part in conceptualisation and writing.

Paper V: I was the principal author, and had the main responsibility for planning the experimental work, SEM/EDX and FIB operation, data evaluation, and writing. The APT measurements and preparation of the APT-tips were performed by Dr. Torben Boll and Delphine Chassaing at Karlsruhe Institute of technology (KIT).

Paper VI: I was the principal author, and the main responsible for SEM/EDX, FIB, XRD and TEM analyses (supervised by Dr. Mohammad Sattari (TEM) and Dr. Johan Eklund (XRD)), as well as data evaluation, conceptualisation, and writing. The TEM was operated mainly by Dr. Mohammad Sattari and partly by me.

Paper VII: I was the principal author, and the main responsible for planning the experimental work, SEM/EDX and FIB operation, data evaluation, and writing. The APT measurements and preparation of the APT-tips were performed by Dr. Torben Boll at Karlsruhe Institute of technology (KIT).

Related publications not included in this thesis:

J. Eklund, B. Jönsson, A. Persdotter, J. Liske, J.-E. Svensson, T. Jonsson, The influence of silicon on the corrosion properties of FeCrAl model alloys in oxidizing environments at 600 °C, *Corrosion Science* 144, 266–276 (2018).

M. A. Olivas-Ogaz, J. Eklund, A. Persdotter, M. Sattari, J. Liske, J.-E. Svensson, T. Jonsson, The Influence of Oxide-Scale Microstructure on KCl(s)-Induced Corrosion of Low-Alloyed Steel at 400 °C, *Oxidation of Metals* 91:291–310, (2019).

E. Larsson, J. Liske, A. Persdotter, T. Jonsson, J.-E. Svensson, L.-G. Johansson, The Influence of KCl and HCl on the High-Temperature Oxidation of a Fe-2.25Cr-1Mo Steel at 400 °C, *Oxidation of Metals* 93, 29–52 (2020).

Contents

1

Introduction

Iron-based alloys are some of the most widely used materials for industrial applications operated at high temperatures. In order to maintain the properties of the materials and maximise component lifetime, the materials used in high temperature applications must resist both mechanical and chemical degradation. The process of degradation of metallic materials at high temperatures is often related to corrosion. Thus, the ability to withstand corrosion is an important aspect of high temperature materials, which is of major concern for many industrial applications.

The challenge of high temperature corrosion of Fe-based alloys is commonly addressed by using high-alloy steels, such as stainless steels, or FeCrAl alloys. The corrosion protection of stainless steels and FeCrAl alloys often rely on the formation of a slow-growing, chromium(Cr)- and/or aluminium(Al)-rich, corundum-type (M_2O_3) oxide scale, which is formed in mildly corrosive conditions [1–3]. However, the presence of corrosive species may result in breakdown of the protective M_2O_3 oxide scales and the formation of a less protective, multi-layered, Fe-rich oxide scale, a process referred to as *breakaway corrosion* [4–25]).

The Fe-rich oxide scales formed after the onset of breakaway corrosion are often considered to be non-protective and may result in catastrophic failure of the material. Nevertheless, in many industrial applications the breakaway event may be difficult to prevent. One example of this is in power plants that combust biomass and waste, where the heterogeneous fuel contains corrosive species, such as chlorine and alkali. The highly corrosive conditions often result in breakaway corrosion of metallic components in an early stage of operation [26–34]. Thus, the corrosion propagation and lifetime of the metallic components in the power plants are determined by the protection of the oxide scale formed after breakaway, which is shown not to be directly related to the properties of the scale formed before breakaway. Therefore, in all applications where breakaway corrosion cannot be prevented, the protective properties of the Fe-rich oxide scale formed after breakaway may be considered important, in particular at intermediate temperatures at which the Fe-oxide scale grows relatively slowly.

In this thesis, the Fe-oxide scales formed after breakaway are studied in detail at intermediate temperatures (400-600 °C). The thesis introduces the concept of primary- and secondary corrosion protection for the oxide formed before and after breakaway. The terminology is considered important for future material research and development, as well as for the selection of materials to be used in applications in which breakaway corrosion cannot be prevented.

The concept is implemented by investigating how the oxide microstructure and oxidation properties of the multi-layered, Fe-rich oxide scale (i.e. the secondary corrosion protection) are affected by the variation in alloy composition, as well as how the oxide scales interact with certain corrosive species that are known to induce breakaway corrosion. The influences of different alloying elements on the secondary corrosion protection are investigated in **Papers I-V** by studying the oxide scales formed after breakaway on Fe-based model alloys that contain varying amounts of Cr, Al, Ni and Si. The impacts of different corrosive species on the secondary corrosion protection are investigated in **Papers IV-VII**) by studying the microstructural changes in the Fe-rich oxides that are formed in different chlorine- and alkali-containing environments.

This work aims to provide insights into what factors that determine the secondary corrosion protection of Fe-based alloys. This is done by examining the following research questions, as discussed in detail in Chapter 5 and **Papers I-VII**:

Q1: What are the main growth mechanisms involved in the formation of a secondary corrosion protection?
Q2. What influences do alloying elements exert on the secondary corrosion protection of Fe-based alloys?
Q3. How do corrosive species influence the growth of the secondary corrosion protection?

In summary,
Paper I investigates the general aspects of the primary- and secondary corrosion protection for a broad range of Fe-based alloys (Q1, Q2).
Paper II studies the influences of Al and Cr on the secondary corrosion protection of FeCrAl alloys (Q1, Q2).
Paper III studies the influences of Ni on the secondary corrosion protection of FeCrNi alloys (Q1, Q2).
Paper IV investigates the long-term corrosion behaviours of FeCrAlSi alloys in slightly more complex environments (Q1-Q3).
Paper V studies the distribution of alloying elements in the inward-growing spinel, and examines how it may influence the protection against corrosive species such as chlorine (Q2, Q3).
Paper VI investigates the general aspects of how corrosive species, such as KCl(s), influence the growth of a multi-layered Fe-rich oxide scale (Q3).
Paper VII studies the distribution and segregation patterns of K and Cl in Fe-oxide, to gain insight to how the corrosive species may interact with the secondary corrosion protection, i.e. the Fe-rich oxide scale formed after the onset of breakaway corrosion (Q3).

General oxidation theory and a description of the methods and experimental techniques used for the investigations are described in Chapter 2-4, to facilitate for the interpretation of the included investigations. The concept of primary- and secondary corrosion regimes are defined in Chapter 2 and implemented in Chapter 5.

2

High temperature corrosion

High-temperature corrosion is one of the most important issues for materials selection and life-time predictions for engineering components exposed to high-temperatures. This chapter focuses on the corrosion of Fe-based alloys exposed at intermediate temperatures (400-600 °C). The chapter includes a short summary of general oxidation theory and descriptions of the oxides that typically form on three important material classes used in high temperature applications: low-alloyed steels; stainless steels; and FeCrAl alloys. This thesis focuses on oxidation of the multi-layered Fe-rich oxide scales that form on these materials in harsh corrosive conditions, i.e., after the onset of 'breakaway corrosion'. This chapter also introduces a new terminology for corrosion of Fe-based alloys at intermediate temperatures, defining the primary and secondary corrosion regimes for corrosion before and after breakaway, respectively.

2.1 General oxidation theory

In general, metal oxidation refers the reaction between oxygen(O) and metal(M) to form a metal oxide (M_aO_b), according to Reaction 2.1:

$$aM(s) + \frac{b}{2}O_2(g) \rightarrow M_aO_b(s). \tag{2.1}$$

The oxidation process is initiated by oxygen anions reacting with metal cations to form oxide nuclei, which grow laterally to cover the entire metal surface. Once the surface is completely covered the formed oxide scale will continue to increase in thickness as long as the reacting species are allowed to pass through the scale. Thus, the formed oxide scale may act as a protective barrier between the metal and the surrounding atmosphere, provided that the oxide scale is slow-growing, continuous, dense, intact, well-adherent, and inert to reactions such as evaporation and melting, such that it hinders the migration of charged species and, consequently, the progression of the oxide growth [1]. Thus, oxidation propagation, and corrosion resistance, are determined by how efficiently this barrier impede the diffusion of charged species through the scale.

The charged species can move through the oxide via bulk diffusion or short-circuit diffusion. Bulk diffusion is determined by the defect structure of the oxide lattice, whereas short-circuit diffusion occurs along microscopic defects, such as cracks, voids and grain boundaries [1,35] (see Figure 2.1). Diffusion is a temperature-dependent process that can be described by the Arrhenius relation:

$$r \propto e^{\frac{-Q}{RT}}, \tag{2.2}$$

where r is the diffusion rate, Q is the activation energy for diffusion, R is the ideal gas constant and T is the temperature (K). The activation energies for short-circuit diffusion paths such as e.g. grain boundaries, are significantly lower than those for bulk diffusion. Given their temperature dependence (Eq. 2.2), the short-circuit diffusion paths become increasingly important at low-to-intermediate temperatures, since the relative rate of bulk diffusion becomes slow.

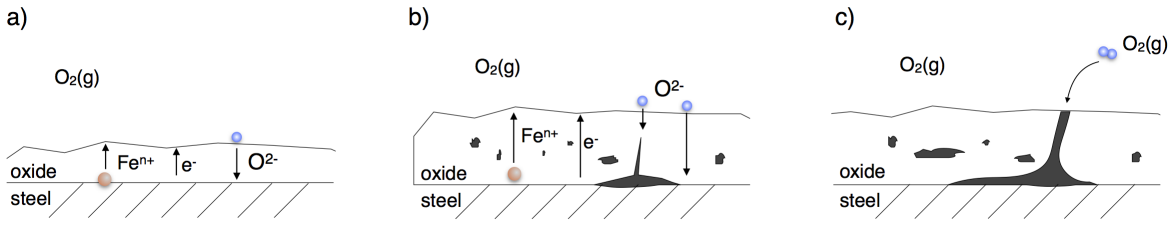

Figure 2.1: Schematic illustration of the process of oxide scale growth through the migration of reacting species through the oxide scale. Migration through the scale occurs via: a) bulk diffusion, b) microstructural defects (e.g., micro-cracks, voids and grain boundaries); and c) macro-cracks and pores.

The oxide scale may grow either by outward diffusion of metal cations (outward-growing scale) or by inward diffusion of anions (inward-growing scale). The outward-growing scale is formed at the gas/scale interface whereas the inward-growing scale is formed at the scale/metal interface (see Figure 2.2a). Many oxide scales grow through both inward- and outward diffusion, and the two different types of scales can be determined by marker experiments. In this work, the presence of Cr in the spinel oxide is used as an indirect marker to distinguish between the inward-growing and outward-growing spinel oxides. This is possible because the diffusion of Cr^{3+} (and Al^{3+}) in the spinel structure is known to be much slower than that of Fe^{2+} (see Figure 2.2b) [36, 37]. Therefore, as soon as the spinel has formed, the Cr ions will remain fixed, resulting in an outward-growing scale containing almost no Cr, providing that the growth is diffusion controlled.

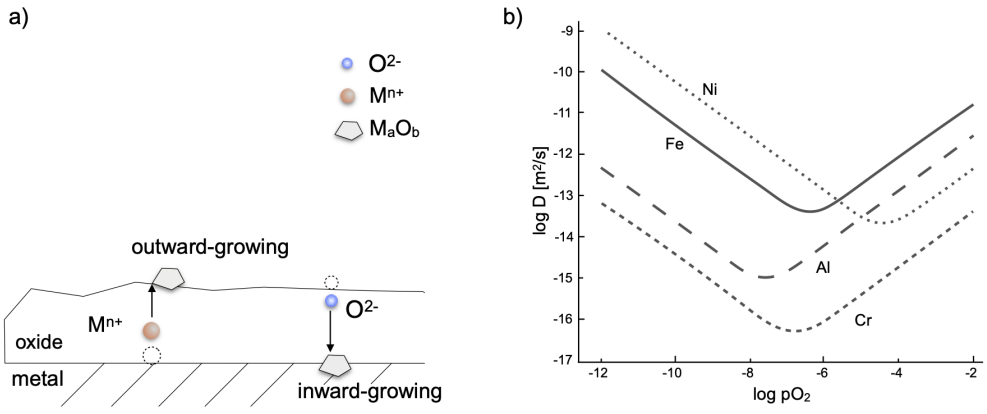

Figure 2.2: a) Illustration of the growth of inward-and outward-growing oxide scales. b) Diffusivities of cations (Fe, Cr, Al, Ni) in Fe_3O_4 at 1200 °C as a function of the partial pressure of oxygen (pO_2). Data for reconstructing the figure were reported by Dieckmann and Schmalzried [38] and summarised by Orman and Crispin [36].

2.1.1 Thermodynamics

Even though the oxide scales studied in this work are not in equilibrium, thermodynamics can be used to explain and predict general aspects of oxide scale growth, in particular at low pO_2 values, where the oxide scale grows slowly. Figure 2.3 and 2.4 show two examples of thermodynamic diagrams that have proven to be useful in the interpretation and prediction of oxidation of Fe-based alloys. The Ellingham diagram shown in Figure 2.3 is useful to illustrate the stability of different oxide systems and gives indications as to which oxides that are expected to form under specific environmental conditions, as well as the expected sequence of oxides in multi-layered oxide scales. The Ellingham diagram can also be used to read off the expected levels of pO_2 at the interfaces between oxides at different temperatures, to allow orientation in the phase diagrams such as that shown in Figure 2.4.

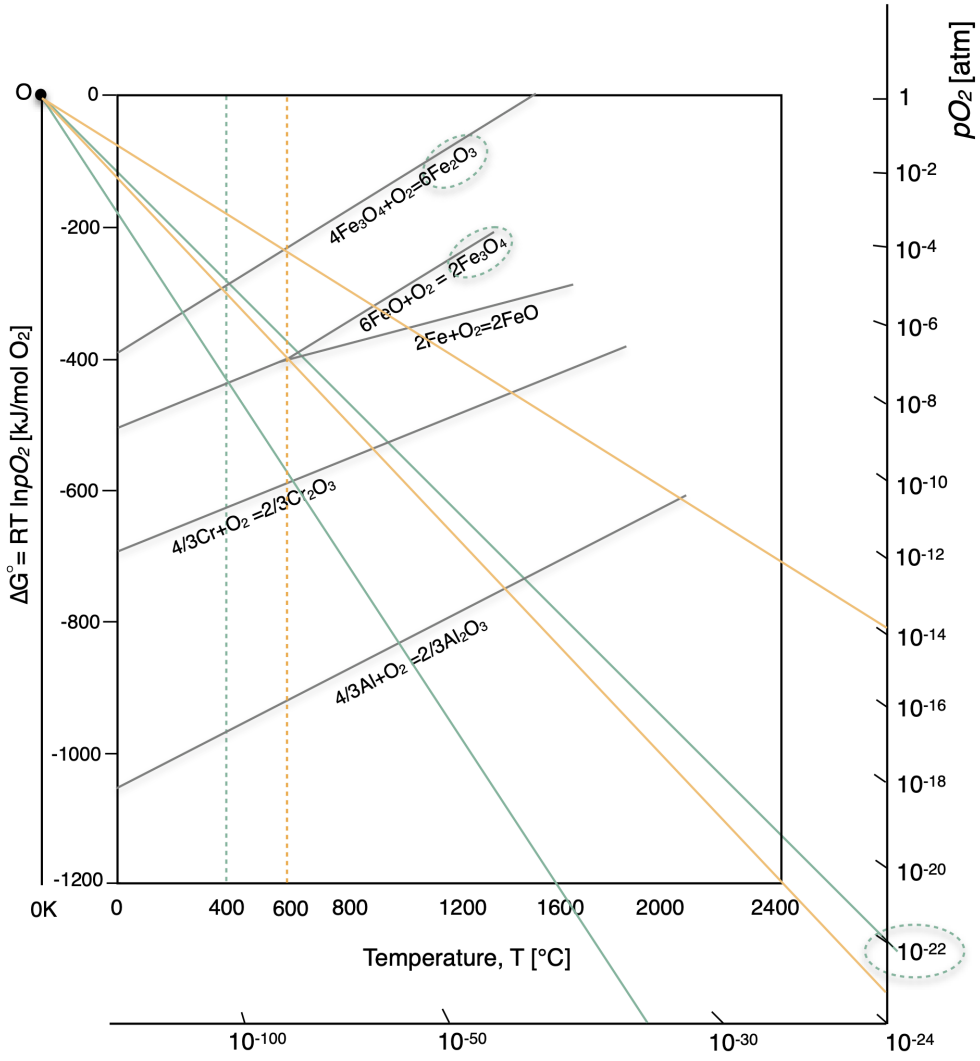

Figure 2.3: Ellingham diagram, reconstructed from data in [1], for a few selected oxides that are relevant to this work. The dissociation pressure (pO_2), above which the specific oxide will form, can be determined graphically for the temperature and oxide of interest. A straight line is drawn from the 'O' point, through the point at which a vertical temperature line crosses the free energy (ΔG) curve for the oxide of interest.

Figure 2.4 shows an example of a phase diagram for a metal-oxide system (FeCrO). This diagram can be used to predict the phases that would form at certain pO_2-levels, i.e., different depth in a multi-layered oxide scale, and concentrations of Cr. The phase diagram reveals miscibility gaps, that result in multi-phase regions of oxides (spinel(S) + corundum(C)), as well as internal oxidation, including metallic phases(M) in combination with oxides (S and/or C). The equilibrium composition can be read from the diagram, as well as the amount of each phase in a two-phase region by using the lever rule.

As can be seen in Figure 2.4 different phases are stable for different Cr-concentrations and pO_2-levels. As we move from high to low pO_2-levels (at low Cr-concentrations), the phase diagram clearly demonstrate the formation of a multi-layered Fe-rich oxide scale, composed of an Fe-rich corundum type-oxide, Fe_2O_3 (C), on top of an Fe-spinel, i.e., Fe_3O_4 (S_{Fe}). At high Cr-concentrations and pO_2-levels only Cr-rich corundum-type oxides (C) are stable. The Cr-rich corundum-type oxides are in general slow-growing, exhibiting excellent corrosion protection at intermediate temperatures, in mildly corrosive conditions (see Section 2.2.1). Thus, this region, and the two-phase region below, containing Cr-rich corundum (C_{Cr}) and Cr-rich spinel (S_{Cr}), are marked as 'protective oxide' in Figure 2.4. At low pO_2 the phase diagram predicts that the alloy would oxidise internally, forming oxide phases (S or C) within the bulk metal (M). These regions are marked 'internal oxidation' in Figure 2.4, and will be discussed in further detail in Chapter 5 (in particular for $10^{-25}<pO_2<10^{-30}$).

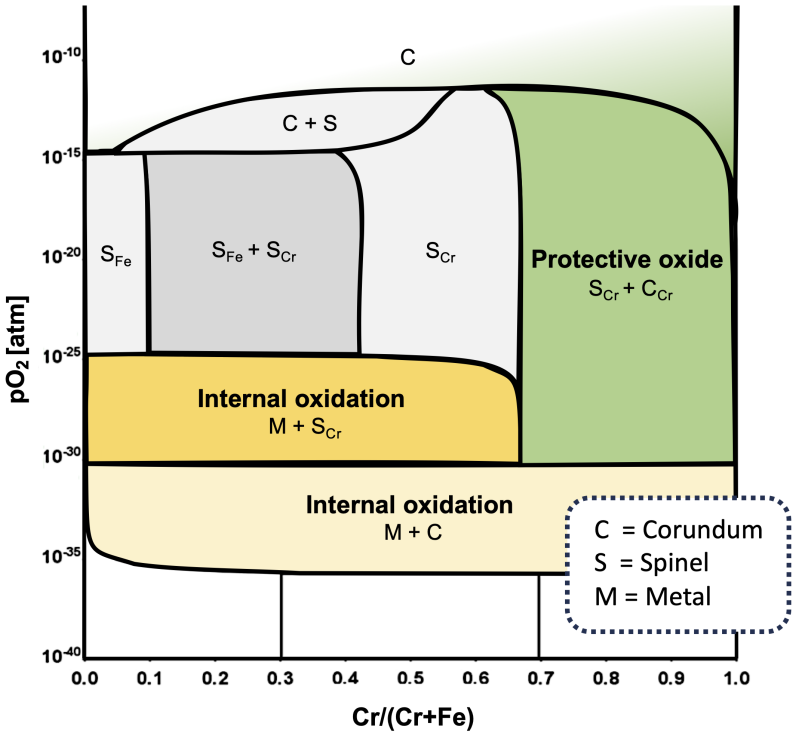

Figure 2.4: Phase diagram for the FeCrO system at 600 °C that can be used to predict the phases that would form at equilibrium for certain pO_2-levels and concentrations of Cr. C_i=corundum-type oxide (i=Fe, Cr), S_i=spinel type oxide (i=Fe, Cr), M=metal (BCC or FCC).

Phase diagrams such as that shown in Figure 2.4 are used throughout this work, in combination with kinetics and microstructural investigations, to increase our understanding as to how alloying elements may influence the growth of the multi-layered Fe-rich oxide scales formed after the onset of breakaway corrosion. In particular, these phase diagrams are used to study the corrosion front, where the system is well-described by thermodynamic phase diagrams in the temperature range studied (400-600 °C). It should be noted that the phase diagram shown in Figure 2.4 is a binary phase diagram (two alloying elements: Cr+Fe). However, more alloying elements can be included by fixing the relative amount of one element in each phase region. As an example, the FeCrNiO system can be evaluated for 10% Ni [x-axis=Cr/(Fe+Cr+Ni)], which would result in a multi-phase region in the position of 'internal oxidation' ($M+S_{Cr}$) in Figure 2.4. The multi-phase region would include an Fe-rich BCC-metal, an FeCr-oxide, and an FeNi-metal, which would contain 10% Ni in total (split between all three phases). Thus, when a third element is included, the composition and amount of each phase in a multi-phase region cannot directly be read from the diagram. Both binary phase diagrams and phase diagrams in which a third element (Al or Ni) is fixed are used throughout this work.

2.1.2 Oxidation kinetics

The rate at which the oxide scale grows, i.e., the oxidation kinetics, is often determined by recording mass changes at different exposure times. This can be done either by continuous thermogravimetric analysis or by several regular furnace exposures that are conducted for different durations. However, the recorded mass changes may also be influenced by other reactions that are not directly linked to the oxide scale growth. Therefore, measurement of oxide scale thickness is a more accurate (albeit more time-consuming) way of determining the growth rates of oxide scales.

The oxidation kinetics are often discussed in terms of ideal rate laws, so as to understand the properties of the oxide scale [1] (see Figure 2.5). Oxide scales formed at high temperatures are commonly assumed to grow according to parabolic kinetics ($x^2 \propto t$, where x is the oxide thickness and t is time), which means that the growth is diffusion-controlled and limited by the transport of charged species through the scale, such that it slows down as the oxide scale grows thicker. The parabolic rate law was derived by Tammann in the 1920's [39] and refined by Wagner in 1933 [40]. Thus, parabolic kinetics is explained by the fact that the oxide scale acts as a diffusion barrier. However, if the diffusion barrier is insufficient, the growth kinetics may be substantially accelerated (see Figure 2.5).

If a protective oxide scale loses its ability to act as a protective barrier, a transition from slow, parabolic kinetics to a more rapid (commonly assumed to be linear) kinetics, a process that is referred to as 'breakaway corrosion' (see Figure 2.5). The breakaway event often results in rapid degradation and catastrophic failure of the material. Thus, the oxide scale formed after breakaway is generally considered to be non-protective, and its formation signals the end of material lifetime. However, this work clearly demonstrate that the growth rate of the oxide scales formed after breakaway on certain materials may be relatively slow at intermediate temperatures (400-600 °C). Thus, the oxide formed af-

ter breakaway may act as a semi-protective scale, a phenomenon that previously has not been received much attention, but that is studied in detail throughout this work.

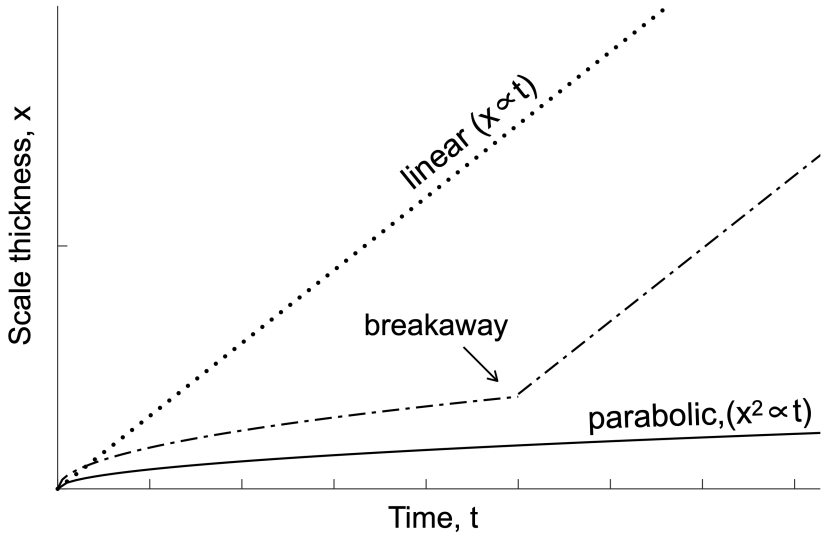

Figure 2.5: Schematic of the ideal rate laws for oxide scale growth at high temperatures: linear growth , parabolic growth, and breakaway oxidation.

2.2 Corrosion regimes in high temperature corrosion

The corrosion protection of stainless steels and FeCrAl alloys often rely on the formation of a slow-growing Cr- and/or Al-rich, M_2O_3 oxide scale, formed in mildly corrosive conditions [1–3]. In severely corrosive condition, these oxide scales tend to break down and a faster-growing, multi-layered, Fe-rich oxide scale is formed, a well-known process referred to as *breakaway corrosion*.

The oxide scale formed after breakaway has previously been studied by several research groups [6, 8, 12, 14, 15, 17, 18, 25]. The oxide scale formed after the onset of breakaway corrosion is considered to be non-protective and the breakaway event often results in rapid degradation and catastrophic failure of the material. Thus, the focus of most of the previous studies has been to increase the understanding, so as to prevent, or delay the Cr/Al-rich M_2O_3 oxide scales from breaking down. As a consequence, studies on the protective properties of the oxide scale formed after breakaway are scarce. Nevertheless, this thesis clearly demonstrate that the growth rate of the scale formed after breakaway may be improved by altering the alloy composition. Thus, the oxide scales formed after breakaway on stainless steels and FeCrAl alloys may act semi-protective at intermediate temperatures ($\sim$ 600 °C). Therefore, in this work, the event of breakaway corrosion is not treated as a stage of failure, but rather as a transition from one type of corrosion regime, **the primary corrosion regime** (before breakaway), to another, **the secondary corrosion regime** (after breakaway), as illustrated in Figure 2.6.

In order to investigate systematically the protective properties of the oxide scales formed after breakaway, this work introduces the concept of primary and secondary corrosion protection for the corrosion protection exhibited of Fe-based alloys before and after breakaway, respectively. The concept is used to study the corrosion behaviour of metallic materials from the perspective of which type of oxide scale that form in a specific environment, rather than from the perspective of the intended corrosion protection for a certain material.

In general, the oxide scales formed before (primary corrosion protection) and after (secondary corrosion protection) breakaway are considered to be fundamentally different, with respect to both the types of oxide scales formed and the growth rates of these oxide scales. The different corrosion regimes are schematically illustrated in terms of oxidation kinetics in Figure 2.6. The primary corrosion regime refers to the growth of a slow-growing, M_2O_3 oxide scale (primary corrosion protection), which may break down, in the presence of for example K_2CO_3, thereby entering the secondary corrosion regime by forming a faster-growing, Fe-rich oxide, i.e., a secondary corrosion protection. The incubation time to breakaway (breakdown of the primary protection), as well as the growth rates of both the primary and secondary corrosion protection may vary for different materials, as illustrated in Figure 2.6. It should be noted that low-alloyed steels do not contain sufficient amounts of Cr or Al to form the primary corrosion protection. Thus, low-alloyed steels form only the Fe-rich type of oxide scale i.e., the secondary type of corrosion protection [1–3].

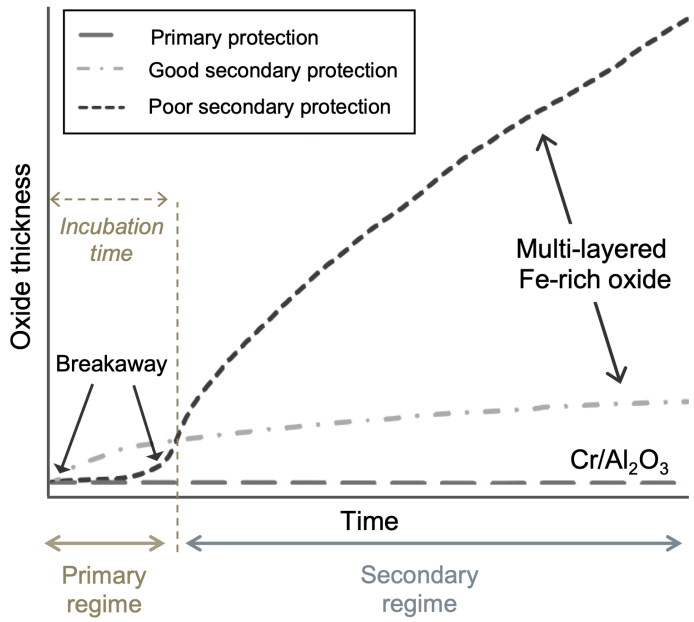

Figure 2.6: Illustration of the primary and secondary corrosion regimes of Fe-based alloys. Slow-growing Cr/Al-rich corundum-type oxides (primary protection) form before breakaway, whereas a multi-layered Fe-rich oxide scale (secondary protection) form after breakaway. The primary and secondary regimes are indicated in the figure along with the breakaway event and incubation time to breakaway. Note that the breakaway event occurs instantaneously for some alloys and that the growth rates may vary significantly for different materials in the secondary corrosion regime.

2.2.1 Primary corrosion protection

The primary corrosion protection of stainless steels and FeCrAl alloys refers to the continuous, slow-growing, Cr- and/or Al-rich, corundum-type (M_2O_3) oxide scale formed in mildly corrosive conditions [1–3]. The corundum-type of crystal structure consists of a hexagonal sub-lattice of oxygen ions with trivalent cations (M^{3+}) occupying two-thirds of the octahedral sites, as illustrated in Figure 2.7 [1]. Chromia (Cr_2O_3), Alumina (Al_2O_3) and hematite (Fe_2O_3), are all corundum-type oxides that can form solid solutions, resulting in mixed M_2O_3 oxides, such as those formed on stainless steels ($(Cr_x,Fe_{1-x})_2O_3$)).

Both the Cr-rich and Al-rich M_2O_3 oxides are comparatively stable at intermediate temperatures (see Ellingham diagram in Figure 2.3), and are considered to be slow-growing oxides due to their low ion mobilities and defect concentration [1]. Provided that the oxide scales are strongly adherent and form continuously over the metal surface, the growth kinetics of both the Cr-rich and Al-rich M_2O_3 oxides are slow and parabolic (i.e., diffusion-controlled, as described in Section 2.1).

Thus, the Cr-rich M_2O_3 oxide scales formed on stainless steels [$(Cr_x,Fe_{1-x})_2O_3$] in mildly corrosive environments exhibit excellent corrosion protection at intermediately high temperatures (<900 °C), while FeCrAl alloys are designed to provide an improved corrosion protection at higher temperatures (>900 °C). The designed corrosion protection of FeCrAl alloys involves the formation of α-Al_2O_3, which mainly exists at temperatures above 900 °C [1, 5, 41]. However, at lower temperatures (<900 °C) the corrosion protection may be attributed to transient aluminas or Al,Cr-rich oxides, with properties similar to the oxides formed on stainless steels [1, 42]. The addition of alloying elements may significantly improve the primary corrosion protection, for example, by facilitating for the formation of a protective Cr-rich and/or Al-rich M_2O_3 oxide scale. The addition of Ni to FeCr-alloys is known to decrease the growth rates, while the addition of Cr to FeAl alloys result in the formation of protective α-Al_2O_3 at lower Al-contents than in the binary alloy (the 'third element effect') [3]. However, in this thesis, the influences of alloying elements are not investigated for the primary corrosion protection, but for the Fe-rich oxides formed after breakaway, i.e., the secondary corrosion protection.

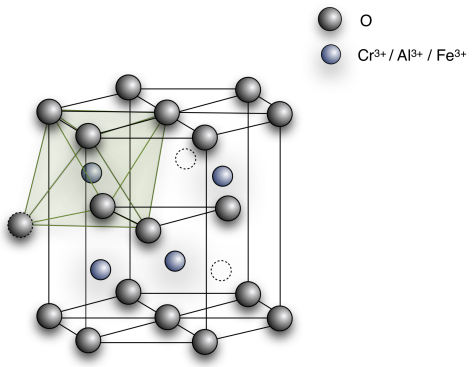

Figure 2.7: Illustration of the atomic distribution in the corundum crystal structures of chromia (Cr_2O_3), alumina (Al_2O_3), or hematite (Fe_2O_3), demonstrating that trivalent cations (Cr^{3+}, Al^{3+}, or Fe^{3+}) occupy 2/3 of the octahedral sites.

2.2.2 Transition from primary to secondary corrosion regime (breakaway corrosion)

The corrosion protection of stainless steels and FeCrAl alloys formed in mildly corrosive environments may, for several reasons, not be sustained in severely corrosive conditions (such as; at high temperatures [4, 9, 43]), or in the presence of water vapour [6, 11–19, 19, 21, 21, 22, 44], alkali, and/or chlorine-containing species [8, 23–25, 44–51]. If the primary corrosion protection (Cr/Al-rich M_2O_3) breaks down, the oxidation proceeds through the formation of a faster-growing, Fe-rich oxide, similar to the oxides formed on low-alloyed steels. This event is often referred to as breakaway corrosion.

Many previous studies have investigated breakaway corrosion and the mechanisms that lead to the breakdown of the Cr/Al-rich M_2O_3 oxide scale, (i.e. the primary corrosion protection) [4–6, 8–10, 12–25, 43, 44, 46–48, 50, 52]. The breakdown mechanisms of the primary corrosion protection are often induced by depletion of the oxide-forming element, caused by an insufficient supply from the alloy substrate. One type of breakdown mechanism for the Cr-rich primary corrosion protection is by **Cr-evaporation**, which may occur, at higher temperatures (>900 °C) through the formation of volatile CrO_3 [53, 54], or in the presence of water vapour through the formation of $CrO_2(OH)_2$ according to Reaction 2.3 [52, 55]:

$$\frac{1}{2}\,Cr_2O_3\,(s) + \frac{3}{4}\,O_2\,(g) + H_2O\,(g) \rightleftharpoons CrO_2(OH)_2(g)\,. \tag{2.3}$$

Another type of breakdown mechanism is Cr-depletion, which is caused by the formation of **alkali chromates** [$(K/Na)_2CrO_4$] in the presence of different alkali-containing species [46, 47] (see for example Reaction 2.4 and 2.5).

$$\frac{1}{2}\,Cr_2O_3(s) + \frac{3}{4}\,O_2(g) + K_2CO_3(s) \rightleftharpoons K_2CrO_4(s) + CO_2(g) \tag{2.4}$$

$$\frac{1}{2}\,Cr_2O_3(s) + \frac{3}{4}\,O_2(g) + H_2O\,(g) + 2\,KCl(s) \rightleftharpoons K_2CrO_4(s) + 2\,HCl(g) \tag{2.5}$$

Thus, the breakdown of the primary corrosion protection may be induced by the presence of a variety of different species (H_2O(g), CO_2(g), KCl(s), K_2CO_3(s)) [6,8,10,47]. Although the breakdown mechanisms may vary depending on exposure conditions, they all result in a similar type of transition from a Cr/Al-rich M_2O_3 oxide scale, to the formation of a multi-layered, Fe-rich oxide scale. The multi-layered, Fe-rich oxide scales have been shown be similar regardless of the environmental conditions [4, 6, 8, 12, 14, 25, 44]. However, as mentioned in Section 2.2, this work clearly demonstrates that the growth rates of the formed multi-layered Fe-rich oxide scales vary for different materials, not directly correlated to the materials performance before breakaway (its primary corrosion protection). Thus, in this work the protective properties of the Fe-rich oxide scales formed after breakaway are studied systematically. The focus remain on the general aspects of the multi-layered Fe-oxide scales formed after breakaway, i.e., the oxidation properties of the secondary corrosion protection. Less attention is paid to the mechanisms causing the breakdown of the primary corrosion protection.

2.2.3 Secondary corrosion protection

The oxide scale formed after breakaway, i.e., the secondary corrosion protection is known to consist of a multi-layered, Fe-rich oxide that is similar to the oxides formed on low-alloyed steels and pure Fe [4, 6, 8, 12, 14, 17, 18, 25, 44]. Low-alloyed steels do not contain enough Cr to form a Cr-rich M_2O_3 oxide scale. As a consequence, the corrosion protection of low-alloyed steels always consists of a multi-layered Fe-rich oxide scale. The multi-layered oxide scales formed on iron, low-alloyed steels, and more highly alloyed Fe-based alloys in the secondary corrosion regime, consist of inward- and outward-growing Fe-rich oxides, as illustrated in Figure 2.8a [56, 57]. The inward-growing scale is a spinel-type oxide (Fe_3O_4 for pure iron and $(Fe_{1-x},M_x)_3O_4$ for alloyed steels) while the outward-growing oxide in general is composed of hematite (Fe_2O_3) on top of magnetite (Fe_3O_4), (and wustite, $Fe_{1-x}O$, at higher temperatures). The layered structure of the multi-layered scale in Figure 2.8a can be explained by the thermodynamic stability of the different oxides and the chemical gradient of oxygen throughout the scale. Thus, the different oxides can be predicted by the Ellingham diagram (see Figure 2.3 in Section 2.1.1) if defects such as voids and cracks are not taken into account [1]. Thus, hematite forms as the top layer of the multi-layered oxide scale (high p_{O_2}), while magnetite, and mixed spinel, form below (lower p_{O_2}) as can be seen in Figure 2.8. Wustite also forms on iron and low-alloyed steels at temperatures above 570 °C (pure iron) [58]. However, wustite is not thermodynamically stable at lower temperatures, and the presence of alloying elements, such as Cr, shifts the equilibrium conditions for this oxide scale to higher temperatures [59]. Thus, wustite is not expected to be observed in this work.

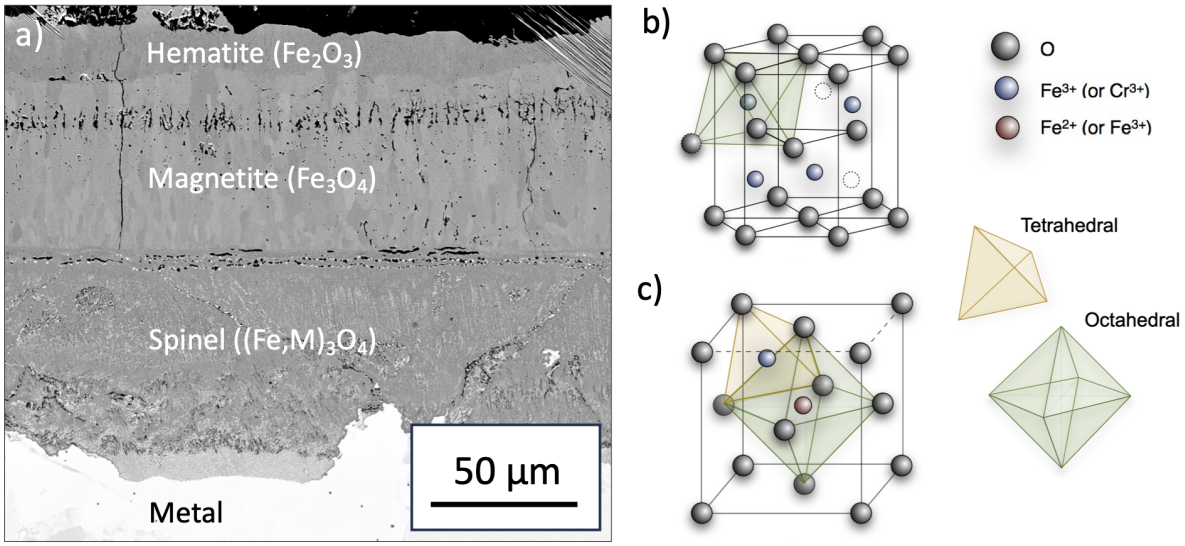

Figure 2.8: a) Characteristic microstructure of the multi-layered, Fe-rich oxide scale formed in the secondary corrosion regime. b-c) Illustration of the atomic distributions of b) hematite (M_2O_3, corundum); and c) magnetite/mixed Fe,Cr,M-spinel (M_3O_4, spinel), demonstrating the tetrahedral and octahedral sites and occupancy for both crystal structures.

Hematite (Fe_2O_3) has a corundum-type crystal structure, similar to those of chromia and alumina, in which the oxygen anions are arranged in a hexagonal array with triva-

lent iron ions (Fe^{3+}) occupying two-thirds of the octahedral sites [58,60] (see Figure 2.8b).

Magnetite, (Fe_3O_4) has an inverse spinel structure [$Fe^{3+}(Fe^{2+}Fe^{3+})O_4^{2-}$], as illustrated in Figure 2.8c, in which the oxygen anions form a face centre cubic (FCC) lattice and the metal cations are positioned in one-eight of the tetrahedral (Fe^{3+}) sites and half of the octahedral sites (Fe^{2+} shared with Fe^{3+}), see Figure 2.8) [58].

The mixed inward-growing spinel, $(Fe,Cr,M)_3O_4$, which is present at the scale/metal interface in Figure 2.8a, has a crystal structure similar to magnetite, albeit with differences in the distribution of divalent and trivalent cations within the octahedral and tetrahedral sites (normal spinel). In the normal spinel, the tetrahedral sites are occupied by divalent ions, while the trivalent ions occupy the octahedral sites [58]. The structure of the mixed spinel ($M^{2+}M^{3+}M^{3+}O_4$) limits the number of divalent and trivalent ions. While Fe^{2+} and Fe^{3+} are both present in and Fe-rich spinel, the oxidation states of Cr, Al and Ni are more restricted (Cr^{3+}, Al^{3+} and Ni^{2+}) [61]. The divalent and trivalent ions have different site preference. Thus, in a mixed spinel, the different alloying elements would not compete equally for the tetrahedral and octahedral sites. Assuming the oxidation states mentioned above, the Fe^{3+}, Cr^{3+} and Al^{3+} would all compete for the trivalent octahedral sites (maximum of 67 at%), while Fe^{2+} and Ni^{2+} would compete for the divalent tetrahedral sites (maximum of 33 at%). Thus, for a mixed FeCrM-spinel, ∼67% of the sites that are occupied by Fe in a pure Fe-spinel could be replaced by Cr^{3+} (corresponding to $FeCr_2O_4$). As mentioned in Section 2.1, the diffusivity of Cr in the spinel is orders of magnitude lower than that for Fe (see Figure 2.2). Thus, providing that the oxide grows by ionic diffusion, the Cr will remain in the inward-growing scale, allowing us to use the distribution of Cr as a marker for the inward-growing scale, which also indicate the original position of the non-oxidised metal surface.

2.2.4 Influences of corrosive species on the secondary corrosion protection

Apart from breaking down the primary corrosion protection, certain corrosive species can affect the overall corrosion process and the growth rate of Fe-oxide scales, i.e., the secondary corrosion protection. In this work, the interactions between the multi-layered, Fe-oxide scales and certain alkali- and chlorine-containing species (K_2CO_3, KCl, HCl) are studied.

Chlorine- and alkali-containing species are well known to accelerate the corrosion of Fe-based alloys [1]. The influence of alkali chlorides and other chlorine-containing compounds has previously been studied extensively for both pure iron [62–66], stainless steels [7, 23, 27, 49, 62–64, 66–76], and low-alloy steels [27, 48, 63, 64, 67, 69, 70, 72, 77–83]. However, the mechanisms underlying chlorine-induced corrosion are still debated. There are several different theories as to how chlorine accelerate corrosion. Grabke et al. [67] suggested that volatile metal chlorides, formed at the scale/metal interface, would diffuse and dissociate to form non-protective porous metal oxides. However, the microstructure of the multi-layered Fe-oxide scales studied in this thesis does not support this theory. Folkeson et al. [80] proposed an alternative mechanism, where chlorides (Cl^-) were sug-

gested to facilitate ionic diffusion by formation of metal chlorides at the grain boundaries. This would result in oxide scales governed by diffusion controlled oxidation, as observed in this study. However, the presence of metal chlorides at the grain boundaries could not be validated.

In this thesis, alkali and/or chlorine containing species are mainly studied to evaluate the capacity as to which the secondary corrosion protection can withstand various corrosive species, and how its presence may influence the microstructure and protective properties of the multi-layered Fe-oxide scales. More extensive mechanistic studies of the influence of each corrosive species remain a topic for future research.

3

Materials and exposures

3.1 Materials

The materials investigated in this thesis are Fe-based model alloys (FeCr, FeCrNi, FeCrAl, FeCrAlSi) and the commercial low-alloy steel Fe2.25Cr1Mo. The material matrices are summarised in Table 3.1, including alloy compositions, crystal structures, and approximate alloy grain sizes. The amounts of Cr, Al, Ni and Si were varied separately for all the model alloys, so as to study the influences of alloying elements on the secondary corrosion protection of FeCr, FeCrNi and FeCrAl(Si) alloys.

The model alloys were produced by Kanthal AB by induction heating and casting in a Cu-mould under an argon atmosphere. The cast cylindrical ingots were machined, prior to hot rolling, to remove surface defects. The cylinders were heated at 1150 °C and subsequently hot rolled into strip samples (13×3 mm) and reheated approximately four times during the process. The samples were heat-treated after hot rolling, in order to achieve a homogeneous grain size. The heat treatments were performed at 950 °C (for 1 hour) for the ferritic alloys and 1050 °C (for 30 min) for the austenitic alloys.

3.2 Sample preparation (pre-exposure)

The delivered model alloys were cut into coupons with sample dimensions that ranged from 8×10×2 mm to 15×15×2 mm. The grain sizes of the alloys were investigated by light optical microscopy (LOM) of chemically etched samples. Chemical etching of the FeCr and FeCrAl model alloys were performed at 60 °C in a solution of HCl/H_2O (50:50), while the etching of the FeCrNi model alloys was performed a a temperature slightly above 60 °C in a solution of $HCl/HNO_3/H_2O$ (45:45:10).

Prior to exposure, the non-etched, metal coupons were ground with SiC paper (P500-P4000), and polished with 1 μm diamond suspensions to achieve a mirror-like appearance. The samples were subsequently degreased in acetone and ethanol using ultrasonic agitation. Two different alkaline salts were sprayed onto the samples prior to exposure (type depending on the investigation), as summarised in Table 3.1.

The alloys examined were sprayed with potassium carbonate (K_2CO_3(s), 1-2 mg/cm^2), dissolved in water (**Paper I-IV**), or potassium chloride (KCl(s), 0.1-1 mg/cm^2) dissolved in ethanol and water (80:20) (**Paper IV-VII**), to induce break down of the primary corrosion protection through the formation of alkali chromates (see Reactions 2.4 and 2.5).

3.3 Furnace exposures

Exposures of the metal coupons were carried out in horizontal tube furnaces. The samples were positioned parallel to the direction of the gas flow. All parts of the system were maintained above the dew-point of water, to prevent condensation. A thermobalance was used to record the mass gain in-situ (thermogravimetric analysis, TGA), providing oxidation kinetics and insight into additional mechanisms such as evaporation and/or crack formation. The thermobalance used in this work was a Setaram Setsys thermobalance, humidified with a Setaram Wetsys (for wet exposures).

The Fe2.25Cr1Mo steel coupons were exposed for 24 hours at 400 °C in 5% O_2 + 20% H_2O + N_2 (bal.) with and without KCl(s) in both the tube furnace and the thermobalance. The model alloys were exposed at 600 °C under oxidising conditions (5% O_2 + N_2), in the presence and absence of K_2CO_3(s), H_2O(g), KCl(s), or HCl(g), for up to 2000 hours. The exposure conditions are listed in Table 3.1.

The gravimetric measurements were carried out using a Sartorius balance with microgram resolution. The estimated oxide scale thicknesses, x, were calculated based on mass gain data (W [g/cm^2]) for each alloy, in order to link the mass gain studies to the microstructural investigations (see Eq. 3.1). The calculations were performed under the assumptions that the oxide scales were dense, composed of one pre-defined oxide (M_aO_b) with density ρ, and that the measured mass gain accounted only for oxygen uptake that resulted in oxide formation.

$$x = \frac{W}{\frac{a M_O}{a M_O + b M_M}\rho} \tag{3.1}$$

The furnace and thermobalance exposures in this work were performed mainly by Dr. Johan Eklund, Dr. Erik Larsson, and MSc. student William Fung. A few exposures were performed by Dr. Mercedez Andrea Olivas Ogaz, Dr. Julien Phother Simon, PhD student Vincent Ssenteza, and BSc. students Emile Sechaud and Fanny Karlsson.

FeCr alloys (model alloys) Exposure gas: 5% O_2 + 95% N_2(g)

Alloy	Cr	Fe	Phase *	Temp.	Salt (+addition)
Fe2.25Cr	2.25	98	BCC	600 °C	- / K_2CO_3(s)(1 mg/cm^2)
Fe10Cr	10	90	BCC	600 °C	- / K_2CO_3(s)(1 mg/cm^2)
Fe18Cr	18	82	BCC	600 °C	- / K_2CO_3(s)(1 mg/cm^2)
Fe25Cr	25	75	BCC	600 °C	- / K_2CO_3(s)(1 mg/cm^2)

FeCrNi alloys (model alloys) Exposure gas: 5% O_2 + N_2 (bal.)

Alloy	Cr	Ni	Fe	Phase*	Temp.	Salt (+addition)
Fe18Cr	18	0	82	BCC	600 °C	- / K_2CO_3(s) (1 mg/cm^2)
Fe18Cr2Ni	18	2	80	BCC	600 °C	- / K_2CO_3(s) (1 mg/cm^2)
Fe18Cr10Ni	18	10	72	50:50 FCC	600 °C	- / K_2CO_3(s) (1 mg/cm^2)
Fe18Cr20Ni	18	20	62	FCC	600 °C	- / K_2CO_3(s) (1 mg/cm^2)
Fe18Cr34Ni	18	34	48	FCC	600 °C	- / K_2CO_3(s) (1 mg/cm^2)
18Cr81Ni	18	81	1	FCC	600 °C	- / K_2CO_3(s) (1 mg/cm^2)
Fe18Cr2Ni	18	2	80	BCC	600 °C	KCl(s) (1 mg/cm^2)+ HCl(g) (500 ppm)
Fe18Cr10Ni	18	10	72	50:50 FCC	600 °C	KCl(s) (1 mg/cm^2) + HCl(g) (500 ppm)

FeCrAl alloys (model alloys) Exposure gas: 5% O_2 + 95% N_2

Alloy	Cr	Al	Fe	Phase	Temp.	Salt (+addition)
Fe5Cr3Al	5	3	92	BCC	600 °C	- / K_2CO_3(s)(1 mg/cm^2)
Fe10Cr3Al	10	3	87	BCC	600 °C	- / K_2CO_3(s)(1 mg/cm^2)
Fe18Cr3Al	18	3	79	BCC	600 °C	- / K_2CO_3(s)(1 mg/cm^2)
Fe18Cr1Al	18	1	81	BCC	600 °C	- / K_2CO_3(s)(1 mg/cm^2)
Fe18Cr6Al	18	6	76	BCC	600 °C	- / K_2CO_3(s)(1 mg/cm^2)
Fe25Cr3Al	25	3	72	BCC	600 °C	- / K_2CO_3(s)(1 mg/cm^2)

FeCrAl(Si) alloys (model alloys) Exposure gas: 5% O_2 + N_2(g) (bal.)

Alloy	Cr	Al	Fe	Si	Phase*	Temp.	Salt (+addition)
Fe10Cr3Al	10	3	87	-	BCC	600 °C	K_2CO_3(s) (2 mg/cm^2)
Fe15Cr3Al2Si	15	3	80	2	BCC	600 °C	K_2CO_3(s) (2 mg/cm^2)
Fe20Cr3Al2Si	20	3	75	2	BCC	600 °C	K_2CO_3(s) (2 mg/cm^2)
Fe10Cr3Al	10	3	87	-	BCC	600 °C	KCl(s) (2 mg/cm^2) + 20% H_2O(g)
Fe15Cr3Al2Si	15	3	80	2	BCC	600 °C	KCl(s) (2 mg/cm^2) + 20% H_2O(g)
Fe20Cr3Al2Si	20	3	75	2	BCC	600 °C	KCl(s) (2 mg/cm^2) + 20% H_2O(g)
Fe10Cr4Al	10	4	86	-	BCC	600 °C	KCl(s)(1 mg/cm^2)+HCl(g)(500 ppm)+20% H_2O(g)
Fe10Cr4Al2Si	10	4	84	2	BCC	600 °C	KCl(s)(1 mg/cm^2)+HCl(g)(500 ppm)+20% H_2O(g)

Fe2.25Cr1Mo (commercial) Exposure gas: 5% O_2 + 20% H_2O + N_2 (bal.)

Alloy	Cr	Mo	Fe	Phase	Temp.	Salt (+addition)
Fe2.25Cr1Mo	2.25	1	bal.	BCC	400 °C	Reference (no chlorine)
Fe2.25Cr1Mo	2.25	1	bal.	BCC	400 °C	+ KCl(s) (0.1 mg/cm^2)

Table 3.1: Exposure matrices and nominal compositions (wt%), and expected crystal structure (phase: ferrite=BCC, austenite=FCC) for all investigated alloys.

3.4 Sample preparation (post-exposure)

After exposure, selected samples were prepared for cross-sectional analyses using scanning electron microscopy (SEM) and transmission electron microscopy (TEM). Sample preparation for SEM/TEM analyses was performed using two different ion-milling tools, namely broad ion beam (BIB) and focused ion beam (FIB). The FIB was also used to image the cross-sections with ions, as described more in detail in Section 4.1.3.

3.4.1 Broad ion beam (BIB)

Broad ion bream (BIB) is a technique used to produce wide, ion-milled cross-sections, so as to generate surfaces that are suitable for surface-sensitive ion and electron microscopy. The technique applies a broad beam of argon (Ar) ions in order to sputter away material from the sample, resulting in millimetre-wide cross-sections. Although, BIB-milling is not as precise as FIB-milling, it allows for analysis of larger areas.

In this work, the BIB was used to prepare wide cross-sections of the Fe-rich oxide scales formed in the secondary corrosion regime. The instrument used was the Leica EM TIC 3X Ion beam milling system equipped with a triple Ar ion gun and operated at 4-8 kV. Higher accelerating voltages (6.5-8.0 kV) were used for coarse milling, while, for some samples, the final milling was performed at 4 kV to generate a better surface for low-keV SEM-imaging. Prior to milling, the samples were cut, without lubrication, using a low-speed saw. The exposed coupons were sputtered with gold and covered with a 0.5-mm-thick silicon wafer prior to cutting, so as to protect the oxide scale from spalling. Preparation of the BIB milled cross-sections in this work was carried out in part by Dr. Johan Eklund, Dr. Erik Larsson and MSc. student William Fung.

3.4.2 Focused ion beam (FIB)

Focused ion beam (FIB) can be used either for microscopy or as a milling tool, as illustrated in Figure 3.1. In this work, the FEI Versa 3D LoVac DualBeam instrument was used to produce well-defined, one-sided cross-sections for scanning electron microscopy (SEM) analysis, as well as electron-transparent lamellae for TEM using the in-situ lift-out procedure described in detail below. The instrument is a combined FIB and SEM (mounted at an angle of 52° relative to each other) that is equipped with a gallium liquid metal ion source (Ga LMIS), detectors for secondary electrons and ions (eSEs, iSEs) and backscattered electrons (BSE), a gas injection system (GIS) for the deposition of platinum (Pt), and an Omniprobe needle for lift-out of the thin TEM lamellae. The GIS is used to inject gas into the sample chamber, directed towards a specific region of the sample, which makes it possible to deposit a protective coating onto the area of interest, as illustrated in Figure 3.1b.

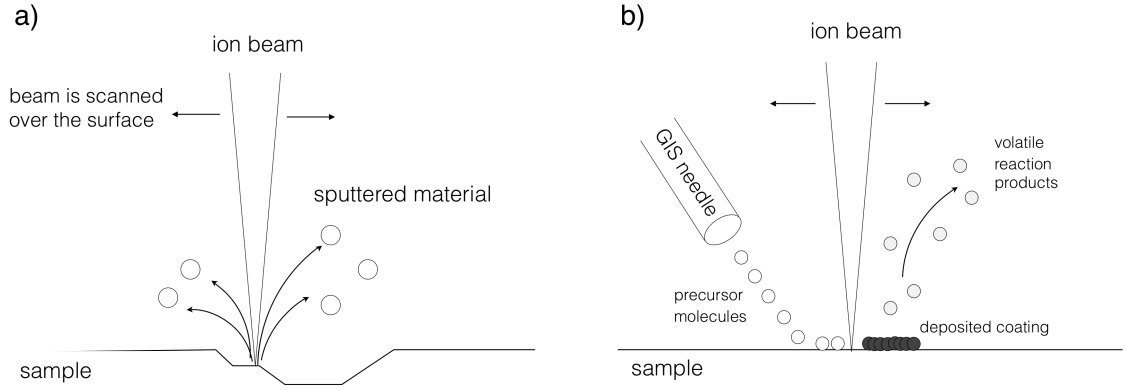

Figure 3.1: Illustration of: a) the milling principle and b) the ion-assisted GIS deposition in the FIB (reconstructed from [84]). The ion beam interacts with a) the sample, to sputter away material; or b) precursor gases (from the GIS) that are adsorbed on the sample surface, so as to generate reaction products that enable the formation of a deposited layer.

The in-situ lift-out procedure used to produce thin lamellae for TEM investigations is illustrated in Figure 3.2. During the lift-out procedure, the electron column was used for monitoring, while the ion column was used for milling. Both the electron and ion column were assisting the GIS for Pt-deposition for sample mounting and specimen protection from ion bombardment, reducing ion implantation and artefacts such as 'curtaining'. The lift-out procedure was carried out in several steps as illustrated in Figure 3.2. A thin, protective Pt-strip was deposited onto the selected region of interest, assisted by electrons (to reduce the risk of ion implantation), and ions (for more efficient deposition), as illustrated in Figure 3.2a-c. The sample was tilted at an angle of 52° (sample surface orthogonal to the ion column) and trenches were milled at high beam currents ($\sim$ 15 nA) on both sides of the Pt-strip (Figure 3.2d). The material beneath and on the sides of the trenches was milled away ('u-cut') with lower beam currents ($\sim$3-5 nA) at a tilt angle of 0° tilt, leaving only one side of the lamella attached to the original sample. The Omniprobe needle was inserted, and Pt was used to mount the other side of the lamella onto the Omniprobe. The remaining material attached to the original sample was removed using relatively low beam current ($\sim$3 nA) ion milling to reduce re-deposition.

The lamella, attached to the Omniprobe needle, was mounted onto a Cu-grid by Pt-deposition. The attachment to the Omniprobe needle was milled away (beam current $\sim$1-3 nA) and the lamella was made thinner in order to produce an electron-transparent specimen ($\sim$ 100 nm in thickness) for the TEM analysis (Figure 3.2e). The thinning of the sample requires careful and precise milling. Thus, the thinning was performed by ion milling using a series of progressively lowered beam currents (1 nA, 0.3 nA, 100 pA) on both sides of the lamella. In the final thinning step (at 100 pA), the milling was performed on both sides simultaneously, in order to reduce the risk of bending of the thin lamella. A final electron-transparent lamella, mounted on a Cu-grid, is shown in Figure 3.2e.

For the preparation of samples to be analysed by means of Atom probe tomography (APT), i.e., APT-tips, the procedure used in this work was similar to that used for the preparation of the TEM-lamellae described above. However, after the lamella lift-out, the

transfer and subsequent thinning steps were different. For the preparation of APT-tip, the lamella was split into pieces, mounted onto posts on an array, and subsequently shaped into cones by annular milling at low beam currents with gradually reduced radii.

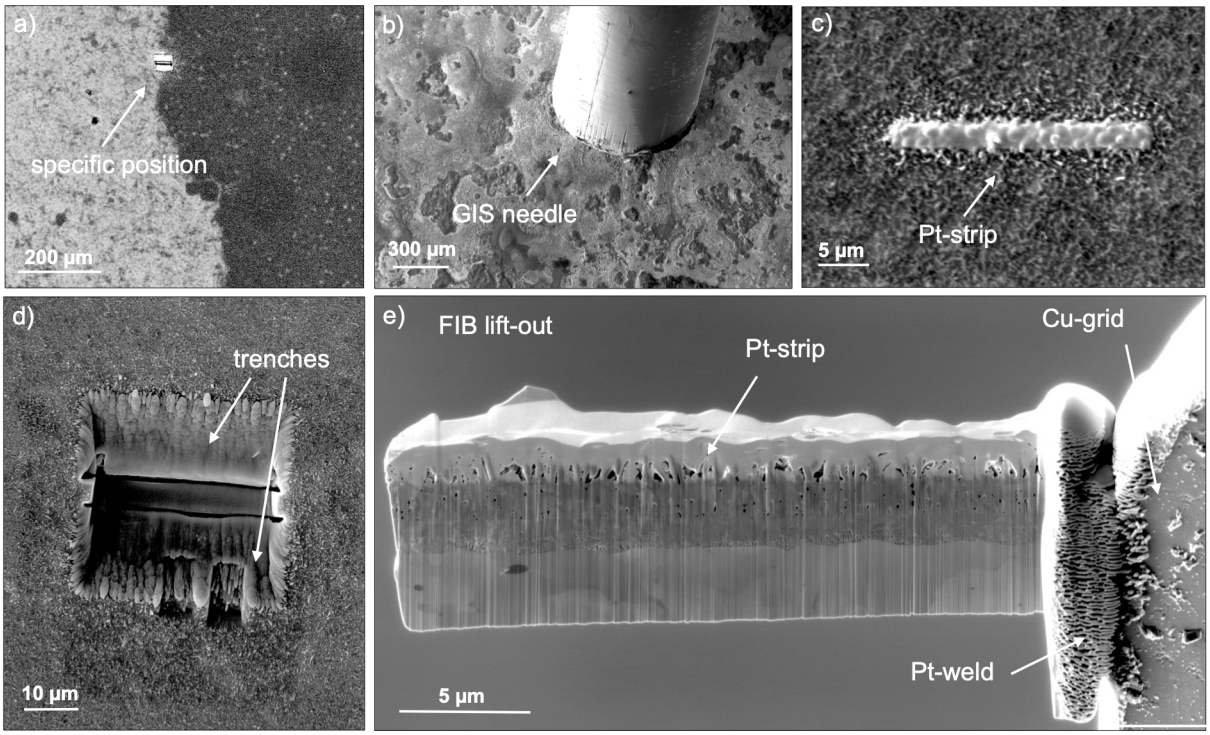

Figure 3.2: Illustration of the lift-out procedure performed in the FIB/SEM system. A precise location is chosen (a), Pt is deposited (b-c), trenches are milled and a thin lamella is extracted and welded onto a Cu-grid (d-e). The specimen is thinned down, resulting in an electron-transparent foil that is suitable for TEM analysis (e).

4

Analytical techniques

The strategy for the microstructural investigations performed in this work is illustrated in Figure 4.1. A combination of characterisation techniques are used to provide complementary data on surface morphology, crystal structure and elemental composition and distribution. The characterisation techniques used cover a wide range of length scales (cm to Å), which enables for detailed characterisation with good statistics.

The oxide scales in this work were analysed using a combination of ion- and electron microscopy techniques (SEM, FIB, TEM), energy dispersive x-ray spectroscopy (EDX), x-ray and electron diffraction (XRD, EBSD, TKD, TEM) as well as atom probe tomography (APT). This chapter presents all the analytical techniques used in the investigation, and briefly explains the underlying physics of the detected signals, to enable the reader to understand and appreciate the specific information obtained from each technique.

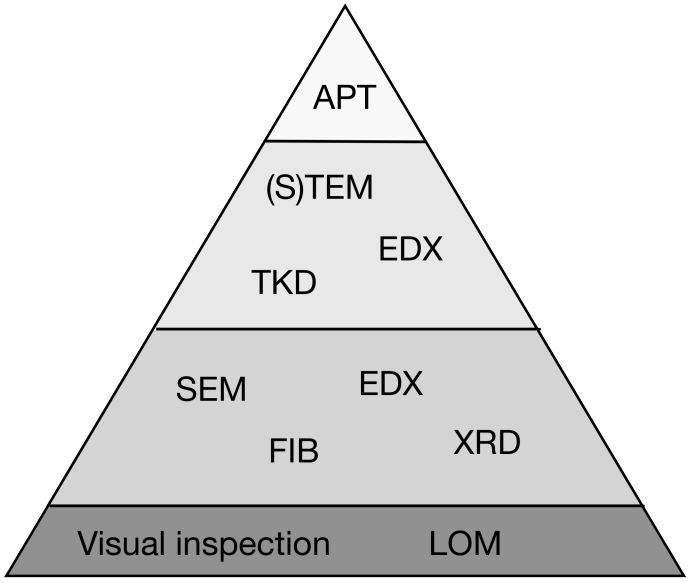

Figure 4.1: Illustration of the strategy used in this work to combine techniques at different length scales (cm to Å) to enable for detailed characterisation with good statistics.

4.1 Imaging

4.1.1 Scanning electron microscopy (SEM)

In scanning electron microscopy (SEM) images are produced by rastering a focused beam of electrons over the sample surface, thereby generating signals that originate from beam-specimen interactions. The signals are detected and converted to obtain high-resolution images, which provide information about the surface topography, density and chemical composition [85]. The high spatial resolution (a few nanometres) and large depth of field are two of the main advantages of SEM compared to light optical microscopy (LOM).

A schematic of an SEM is presented in Figure 4.2. The SEM comprises three main parts: 1) the electron gun, positioned in the top of the electron column, in which the electron beam is generated and accelerated; 2) the lens system (through the electron column) where the beam is controlled by electromagnetic lenses and apertures; and 3) the sample chamber, in which the electron-specimen interactions are detected. To obtain high-quality images in the SEM, the electron beam must be focused onto the sample, with the smallest possible probe size, while maintaining a high electron current. This is achieved by using a set of electromagnetic lenses and apertures through which the accelerated electrons pass before reaching the specimen. The main electromagnetic lenses in the electron column are the condenser lens and the objective lens, while scanning coils are used to raster the beam over the specimen. The condenser lens converges the electron beam to obtain a small probe size, while the objective lens is used to focus the electron beam onto the sample [85].

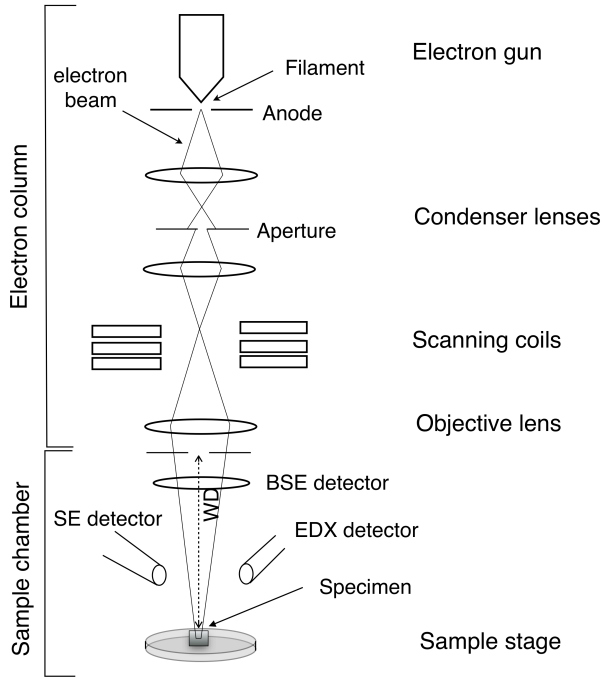

Figure 4.2: Schematic of an SEM. The figure is composed from the descriptions in [85]. Note that the design and beam cross-over may differ depending on the type of SEM used.

The beam-specimen interactions in the SEM generate various types of signals. In this work, the secondary electrons (SEs), backscattered electrons (BSEs) and characteristic x-rays are used (and diffraction, as further discussed in Section 4.3.2). The signals are detected from different depths of the specimen, as illustrated by the interaction volume in Figure 4.3. This is explained by the fact that SEs, BSEs and characteristic x-rays have varying abilities to escape from the specimen, i.e., different escape depths, resulting in varying spatial resolutions for the different signals.

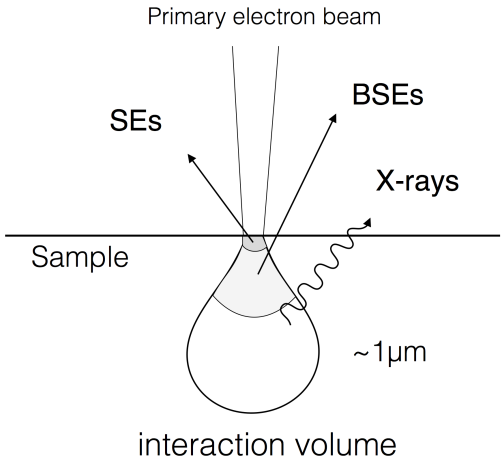

Figure 4.3: Illustration of the interaction volumes of some of the detected signals in the SEM. The size and shape of the interaction volume depend on the specimen and accelerating voltage. However, it is in the order of ∼1µm for characteristic x-rays at 20 keV in Fe.

The **secondary electrons (SEs)** are low-energy electrons (<50 eV), that are ejected from the specimen (see Figure 4.4a). The small interaction volume of SEs (short escape depth, see Figure 4.3) results in surface sensitive images with a spatial resolution of a few nanometers. The short escape depth also results in enhanced topographical contrast in SE-images, due to the so-called 'edge effect'.

The **backscattered electrons (BSEs)**, on the other hand, are elastically scattered electrons (see Figure 4.4b), with energies similar to those of the primary electrons (in the order of keV). Thus, the BSEs can escape from greater depths in the specimen, resulting in poorer spatial resolution (a few hundred nanometres). The number of BSEs generated is proportional to the atomic number (Z) and the density of the sample [85]. Thus, the BSE images contain information about both density and composition, reflected as brighter (dense/higher Z) and darker (porous/lower Z) regions in the image. In this work, the compositional contrast of BSEs is also used for qualitative determinations of the thicknesses and distributions of oxide scales grown on the metal coupons. If the accelerating voltage is set high enough for the interaction volume to reach the metal substrate beneath the oxide, a thin oxide scale will result in more BSEs being generated from the metal substrate. Thus, the BSE contrast results in images with brighter regions for thin, as compared to thick, oxide scales.

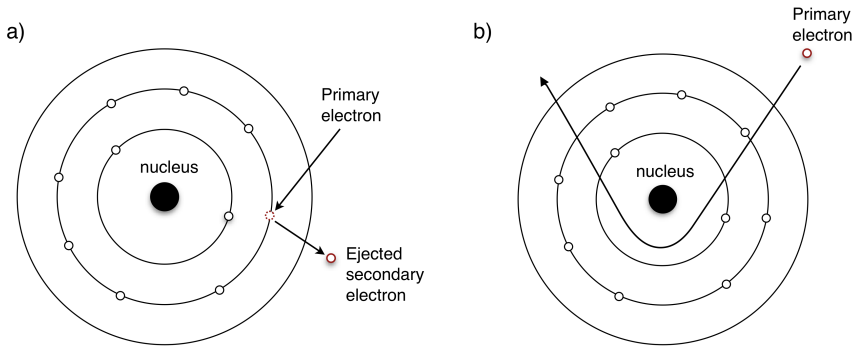

Figure 4.4: Illustration of the principles underlying the generation of: a) secondary electrons (SEs); and b) backscattered electrons (BSEs), based on the description in [85].

In this work, the SEM was used in combination with Energy dispersive x-ray spectroscopy (EDX) to investigate the morphology and composition of the surface, as well as to examine the wide cross-sections prepared by BIB milling. The SEM analysis is of great importance in ensuring that the samples chosen for TEM, or APT, analysis are representative of the overall corrosion of the samples. The SEM analysis was performed on the FEI Quanta ESEM 200, the FEI Versa 3D LoVac DualBeam and the Zeiss LEO Ultra 55 FEG SEM, all operated in high vacuum mode. All three microscopes were equipped with field emission guns and operated at accelerating voltages in the ranges of 1.5-2.0 keV, for surface-sensitive imaging in the Zeiss LEO Ultra 55 FEG SEM, 10-30 keV, for SEM-imaging in the FEI Quanta ESEM 200 and Versa3D, and 15-20 keV for the chemical analysis (EDX). Both secondary electrons (SEs) and backscattered electrons (BSEs) were used for imaging.

4.1.2 Transmission electron microscopy (TEM)

Transmission electron microscopy (TEM) has the ability to provide imaging and chemical analysis with high spatial resolution, as well as site-specific crystallographic information about the sample studied [86]. The principle of imaging in the TEM is different from that of the SEM in that the image is formed by the electrons that are transmitted through the specimen. In order for the electrons to pass through the specimen, the samples need to be electron-transparent (thickness of ∼100 nm) at the operating accelerating voltage (∼ 300 keV).

The TEM can be operated either in conventional TEM mode or in scanning TEM (STEM) mode. The general schematic design of the TEM is rather similar, albeit more complex, to that of the SEM and FIB, in particular in STEM mode. The primary electrons are generated and accelerated in the electron gun and pass through a set of electromagnetic lenses, apertures, and scanning coils (for STEM), before reaching the sample. In contrast to the SEM and FIB, the electron interactions for imaging in the TEM are detected below the sample where the transmitted electrons pass through additional electromagnetic lenses to further magnify the image [86].

The transmitted electrons either pass straight through the sample or are scattered within the sample, enabling different imaging modes (see Figures 4.5 and 4.6). The imaging mode for detecting un-scattered electrons is called **bright-field (BF) mode**. In BF-mode, the image is produced by the un-scattered electrons, and the scattered electrons are efficiently filtered out by the objective aperture. This results in images, in which regions that give rise to less electron scattering appear brighter, e.g., thinner regions, pores, or elements of lower atomic number (see example Figure 4.5a) [86]. In contrast, in the **dark-field (DF) mode** images are created by the scattered transmitted electrons, such that thin areas and pores, which scatter fewer electrons, will appear dark, while denser regions or materials with higher atomic numbers will appear bright.

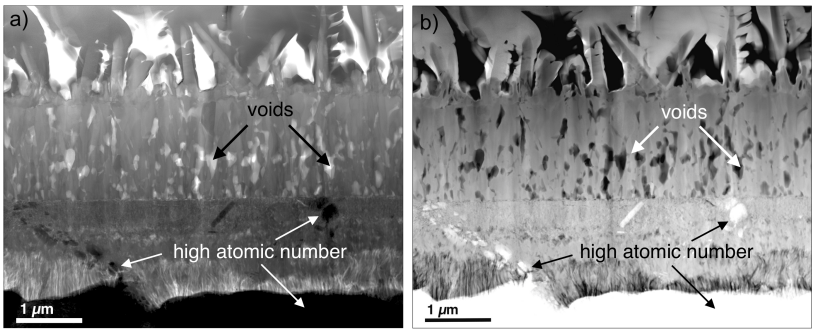

Figure 4.5: Examples of a) bright-field imaging and b) dark-field imaging using STEM. The TEM images were captured by Dr. Mohammad Sattari.

Different detectors are used to detect the scattered transmitted electrons and to enhance certain contrasts. In STEM mode, a DF-image may be produced by an annular dark field detector (ADF), which is sensitive to scattered electrons from a specific range of angles (see Figure 4.6). The scattering intensities at high scattering angles are strongly dependent upon the atomic number, which results in enhanced compositional contrast for high scattering angles, with heavier elements appearing bright, in contrast to the BF-imaging mode [86]. This is the working principle of the High-Angle Annular Dark-Field (HAADF) detector (see Figure 4.5b).

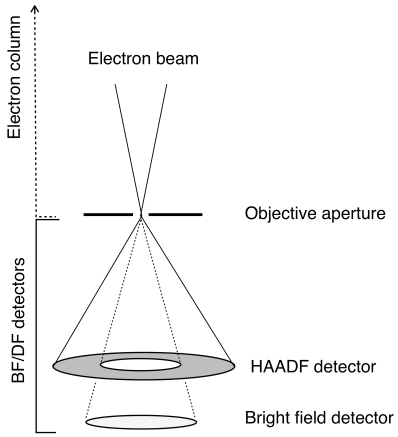

Figure 4.6: Schematic of the BF and HAADF detectors in the TEM (generated from description in [86]).

In this work, an FEI Titan 80-300 TEM was used, equipped with a field emission gun, and an Oxford X-sight EDX detector. The TEM was used in both TEM and STEM mode, using BF and HAADF imaging modes. High resolution TEM (HR-TEM) imaging was performed for visualising the size of crystallographic domains. The chemical analysis performed in the TEM was performed by using STEM/EDX analysis.

4.1.3 Focused ion beam (imaging mode)

The principle of the FIB used as a microscope (imaging mode) is similar to that of the SEM (see section 4.1.1), with the difference being that the FIB uses ions, instead of electrons, as the incident beam. The resolution of the FIB is in the same order of magnitude, albeit slightly lower than that of the SEM. The design of the FIB is similar to that of the SEM. Thus, ions are generated by an ion source (Ga LMIS) and pass through a set of electrostatic lenses and scanning coils, so as to focus and raster the ion beam onto the sample (see Figure 4.7a) [87, 88].

The FIB used in this work was an FEI Versa 3D LoVac, which is a DualBeam instrument, combining a FIB and an SEM, whereby the electron column and the ion column are mounted at an angle of 52° relative to each other (see Figure 4.7b). Imaging in the FIB/SEM workstation can be performed either using an incident ion beam (FIB) or an electron beam (SEM), as illustrated in Figure 4.7. The incident ion beam interacts with the specimen, resulting in emitted SEs (iSEs) and secondary ions (iSIs), which can be detected to form an image [87]. Imaging with iSEs is a commonly used imaging mode in the FIB, due to its higher spatial resolution and yield, compared to iSI-imaging [87, 88]. However, the spatial resolution of ion-induced SEs is still lower than that of electron-induced SEs (eSEs).

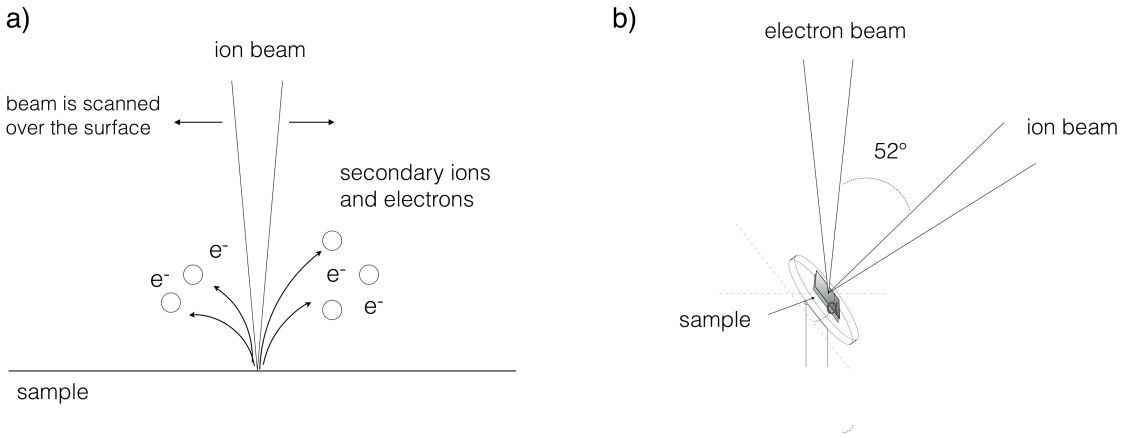

Figure 4.7: Illustration of the image formation in the FIB (a), as reconstructed from [84], and b) a schematic of the SEM/FIB workstation.

The drawbacks of using FIB in imaging mode include its lower spatial resolution, as compared to SEM, and the fact that it is a destructive technique. The highly energetic incident ions will sputter away material from the sample and may cause ion implantation even at low beam currents. However, an important advantage of FIB used for imaging is that a contrast mechanism called 'channelling contrast' is enhanced in ion microscopy (see example in Figure 4.8b). Channelling contrast is based on the principle that crystal lattice planes aligned with the ion trajectory will channel more ions, resulting in a lower SE yield. Thus, when imaging polycrystalline samples, the channelling contrast will produce images, in which the grains that are oriented in the ion trajectory appear darker (low SE yield), while the grains that are in other orientations appear brighter (see example in Figure 4.8a-b) [84, 87].

In this work, FIB-imaging was primarily used to image the oxide grains. The instrument was operated in high-vacuum mode at an acceleration voltage of 30 keV and a beam current of ∼10 pA. In order to obtain better grain contrast, the cross-sections were imaged several times in a row using iSEs. The repeated ion imaging result in ion-etching of the oxide grains, which may be used as an additional sample preparation technique for imaging small oxide grains with low-keV SEM (see Figure 4.8c). The oxide grain sizes, reported throughout this work, are measured in an orientation that is orthogonal to the oxide growth direction, assuming that these grain boundaries are the most relevant pathways for ion diffusion through the oxide scale.

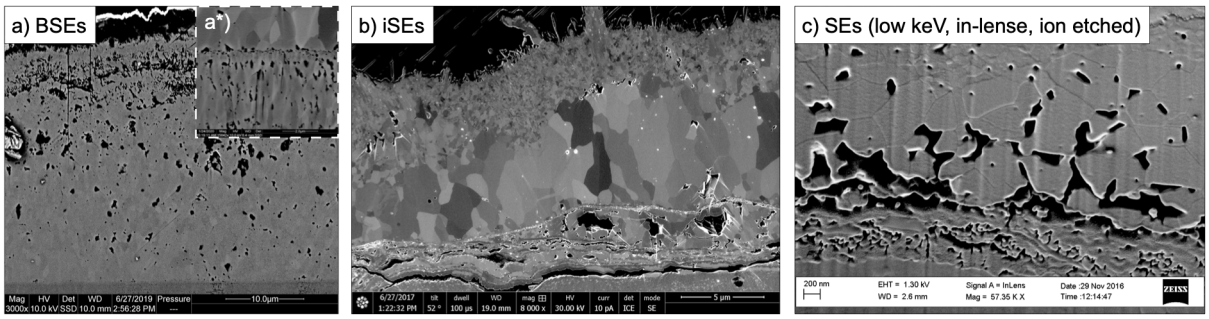

Figure 4.8: Examples of different techniques used to image oxide grains. a) BSE imaging (channelling contrast), b)iSE imaging (enhanced channelling contrast), c) low keV SE-imaging on an ion-etched surface. The insert in a) shows how an improved surface may enable for better grain contrast also in BSE mode (a).*

Tilting the sample may enhance the channelling contrast. However, when producing images of tilted samples, the tilting angle, relative to the electron or ion column, must be taken into account. If the microscope is not equipped with automatic tilt-correction the thickness of the oxide scale, or grain size, measured in the image must be re-calculated using Eq. 4.1,

$$T = \frac{T_0}{\sin\theta} \tag{4.1}$$

where T is the true thickness, T_0 is the measured thickness (image), and θ is the tilt angle (relative to the horizontal plane) (see Figure 4.7b). Note also that when imaging a cross-section that is milled at an angle, the cut may result in that columnar oxide grains are misinterpreted to be equiaxed.

4.2 Chemical analysis

4.2.1 Energy dispersive x-ray spectroscopy (EDX)

Energy dispersive x-ray spectroscopy (EDX) is a powerful tool for chemical analyses of oxide scales [85, 86]. EDX uses characteristic x-rays, which are generated when the primary electron beam interacts with the specimen, as illustrated in Figure 4.9. The primary electrons eject low-energy (inner shell) electrons from the specimen, thereby exciting the atom. The atom relaxes by that an electron from a higher energy level (outer shell) re-occupies the electron position at the lower energy level, during which process characteristic x-rays may be generated. The generated x-rays have specific energies that corresponding to the difference between the two energy levels, and are characteristic of the atom from which they are generated. The beam-specimen interactions will not only generate characteristic x-rays, but will also generate a continuous x-ray spectrum (bremstrahlung), as a consequence of the interactions with free and loosely bound electrons that will slow down the primary electrons. Thus, the generated x-ray spectrum contains both the bremstrahlung (background) and the discrete characteristic x-ray lines (see example in Figure 4.9).

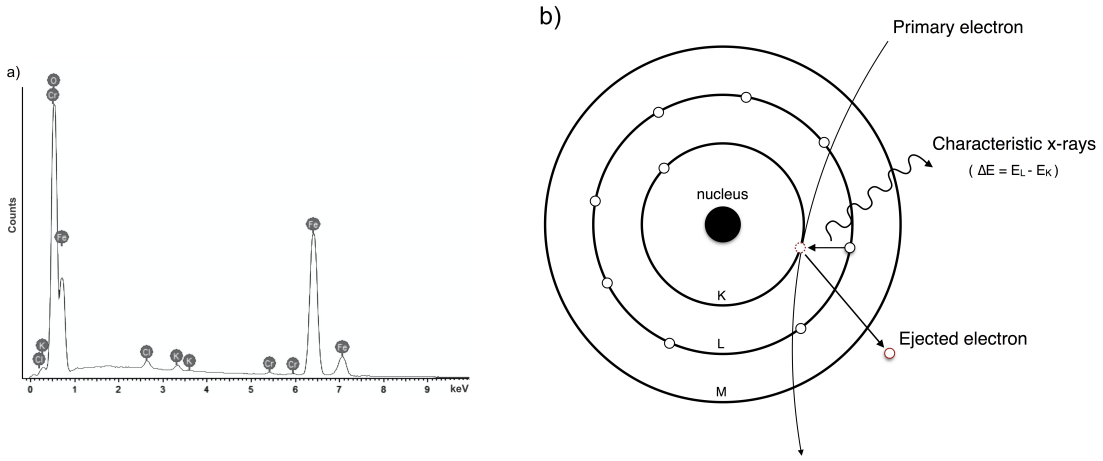

Figure 4.9: Illustration of EDX analysis; a) Example of an EDX-spectrum, b) Illustration of the generation of characteristic x-rays used for EDX analysis.

Characteristic x-rays can escape from a larger volume of the sample, as compared to SEs or BSEs, resulting in that EDX analysis in the SEM has a poorer spatial resolution, as illustrated in Figure 4.3 [85]. The size of the interaction volume in the SEM depends on both the type of specimen and the accelerating voltage, with lower accelerating voltages resulting in smaller interaction volumes. However, the accelerating voltage must still be sufficiently high to eject the inner shell electrons, so as to generate the characteristic x-rays. In STEM/EDX analysis, the sample thickness of the TEM lamella results in a significantly smaller interaction volume, enabling for EDX analysis with higher spatial resolution. The spatial resolution of the STEM/EDX analysis is within the order of nanometres, as compared to the micrometre resolution obtained on bulk samples in the SEM/EDX [86].

Quantitative EDX analysis is performed by filtering out the background signal and integrating the area of the characteristic x-ray peaks. The accuracy of quantitative EDX analysis depends on several factors, including x-ray yield, sample homogeneity, data processing and errors associated with the standards used for the quantification [85]. The ZAF-correction is commonly used in order to compensate for some of the factors, such as the effects of electron scattering for different atomic numbers (Z), the the absorption of x-rays within the specimen (A), and the fluorescence effect (F) that results from that generated x-rays from one type of atom excites surrounding atoms.

In the STEM/EDX, the thin samples result in reduced absorbance and fluorescence effects, which is used in the thin-foil criterion, thereby simplifying the quantification by assuming that factors A and F can be neglected [86]. However, it is noteworthy that the absorbance and fluorescence effects are enhanced for thicker specimens (thicker TEM-lamellae), and that different atoms may be more or less sensitive to the above-mentioned factors. The corrections for accurate quantification in STEM/EDX-analysis are often not suited for heterogeneous samples, for example heavily porous oxides, in which the lamella-thickness vary for different regions. Thus, in both the STEM/EDX and SEM/EDX analyses, caution must be exerted in the quantification. If possible, a sample of known composition, should be quantified as a reference before starting the EDX analysis. Another aspect of the EDX analysis, that needs to be considered, is that the quantification of lighter elements, such as e.g., oxygen, may be inaccurate. Thus, in this work, oxygen is to a large extent excluded from the quantification, and only cations are quantified. An alternative strategy to this problem is to perform a standard EDX analysis, to obtain a better quantification of, for example oxygen, using known standards and non-normalised quantification.

In this work, EDX is used both in the SEM and (S)TEM, resulting in chemical analyses that have different spatial resolutions, due to the reduction in interaction volume that occurs when switching from bulk (SEM) to thin-foil (TEM) samples. Thus, the chemical analysis is more local for the STEM/EDX than for the SEM/EDX. There are both advantages and disadvantages associated with the deployment of each of these techniques, and a combination of the two techniques provides complementary information. The EDX detector used in the SEM was an Oxford X-max 80 EDX, while an Oxford X-sight EDX detector was used in the TEM. The quantification was performed in the Oxford Aztec and Oxford Inca software for the SEM/EDX, and the TIA software for the STEM/EDX.

4.2.2 Atom probe tomography (APT)

Atom probe tomography (APT) allows for three-dimensional visualisation of the chemical composition at sub-nanometre resolution. The sensitivity is in the range of parts per million (ppm) for all elements (including light elements), making APT a valuable complement to x-ray spectroscopy tools, such as EDX. The technique, schematically illustrated in Figure 4.10, is destructive in nature and is based on removing ions from the specimen surface through field evaporation that is induced by laser or high-voltage pulsing. The ions pulled from the surface (specimen tip) are detected on a position-sensitive detector, where the x and y positions of the ion hits are recorded, as well as the order of arrival, and time of flight for the ions to reach the detector. This information can be used to obtain mass-to-charge ratios that is used for a reconstruction to distinguish what ions are present at the specific position of the specimen. The field evaporation requires a strong electrostatic field, which is why APT samples are prepared into very sharp tips (radius <100 nm) [89]. As described in Section 3.4.2, the APT-tips in this work are prepared in a similar manner to the TEM lamellae, with additional extraction of pieces for subsequent tip shaping. The sample can be chosen from the exact region of interest, either in bulk or surface.

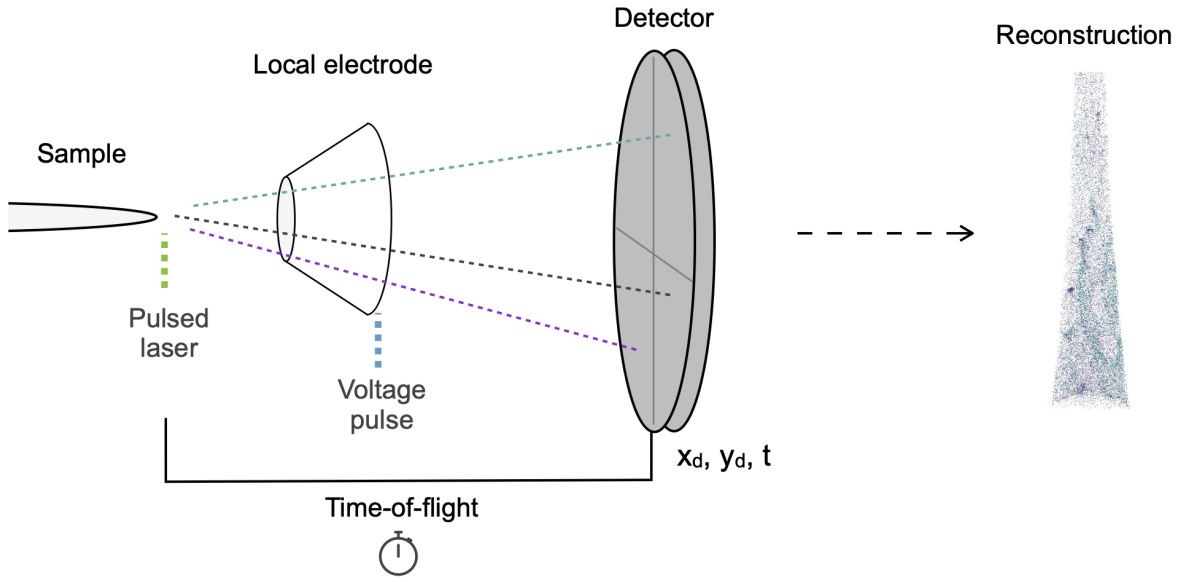

Figure 4.10: Schematic illustration of the working principle of APT, based on descriptions in [89].

In this work, the APT measurements were performed by Torben Boll at Karlsruhe Institute of Technology (KIT). The instrument used was a Cameca Local Electrode Atom Probe (LEAP) 4000X HR, at a set temperature of 60 K, a laser pulse energy of 30 pJ, an evaporation frequency of 100-200 kHz and a detection rate of 0.3-0.5 %. The three-dimensional atom maps were reconstructed based on SEM images and evaluated with IVAS 3.6.14 and 3.8.14. Similar to the EDX analysis, oxygen is excluded in the reported quantification, unless stated otherwise.

4.3 Diffraction

4.3.1 X-ray diffraction (XRD)

X-ray diffraction (XRD) is used to determine the crystal structures of crystalline materials [90]. The technique is based on the Bragg diffraction resulting from incident x-rays that interact with the crystal lattice. Bragg diffraction occurs at discrete angles according to Bragg's law: $2d \sin\theta = n\lambda$, where n is a discrete integer, θ is the incident angle, λ is the x-ray wavelength, and d is the distance between the atomic planes in the crystalline material. By measuring the angles and intensities of the Bragg diffracted beams, the crystal structure of the sample can be determined. In the present work, oxide crystal structures were characterised using the Siemens D5000 powder x-ray diffractometer with a CuK_α source (λ=1.5418 Å). The instrument was operated in grazing incidence geometry with an angle of incidence between 0.5 - 4.0°, and a measuring range of $10° < 2\theta < 85°$. The XRD measurements in this work were performed with the assistance of Dr. Johan Eklund at Chalmers University of Technology.

4.3.2 Electron diffraction (EBSD, TKD and TEM)

In addition to their application in imaging and chemical analyses, the electron interactions that take place in crystalline materials also result in electron diffraction according to Bragg's law (see above Section 4.3.1), where λ refers to the de Broglie wavelength of the electrons). Thus, the SEM and TEM allow for the detection and visualisation of the crystal structures, and for example, grain orientations of polycrystalline materials. In the SEM, the crystallographic information and grain orientation can be obtained by electron backscatter diffraction (EBSD) or transmission Kikuchi diffraction (TKD). Both techniques are based on the same principle and use the same type of detector. However, EBSD is performed on bulk samples, which means that the resolution is limited by the electron interaction volume, whereas TKD is performed on thin-foil samples [91]. In the TEM, two different diffraction modes are possible: i) selected area electron diffraction (SAED); and ii) convergent beam electron diffraction (CBED), producing spot-based and disc-based diffraction patterns, respectively [86]. In this work, electron diffraction was used in order to confirm the presence of different oxide phases in different regions of the oxide scales as well in a qualitative manner to determine whether or not certain regions were crystalline. The EBSD and TKD analysis were performed using a Tescan Gaia3 equipped with a NordlysNano Camera. The instrument was operated at 20 kV to obtain the Kikuchi patterns necessary for phase determination. The TKD and EBSD were operated by Pat Trimby at Oxford Instruments and Dr. Johan Eklund, respectively.

5

Results & discussion

The corrosion protection of stainless steels and FeCrAl alloys often rely on the formation of a slow-growing Cr- and/or Al-rich M_2O_3 oxide scale, i.e., the primary corrosion protection. However, in corrosive conditions, these oxides tend to break down, resulting in the formation of a fast-growing, multi-layered, Fe-rich oxide scale, a well-known process referred to as breakaway corrosion. The oxide scales formed after breakaway are often considered to be non-protective and previous studies have mainly focused on how to delay, or prevent, the breakaway event. Nevertheless, in many industrial applications the breakaway event may be difficult to prevent. Thus, the corrosion propagation and lifetime of metallic components exposed under corrosive conditions are often determined by the protection of the Fe-rich oxide scale formed after breakaway.

Therefore, this thesis, investigates systematically the protective properties of the Fe-rich oxides formed after breakaway, i.e., the secondary corrosion protection (see Section 2.2.3) at intermediate temperatures (400-600 °C). This is done through well-controlled breakdown of the Cr/Al-rich corundum-type oxide, i.e., the primary corrosion protection (see Section 2.2.1). The formed multi-layered Fe-rich oxide scales are subjected to detailed microstructural investigations, to elucidate how the properties and microstructure of the Fe-rich oxides change as a result of altered alloy composition, and/or the presence of certain corrosive species.

The influences of different alloying elements on the multi-layered Fe-rich oxide scale, i.e., the secondary corrosion protection, are investigated in **Papers I-V** and summarised in the following sections. The influences of more corrosive species are studied in **Papers IV-VII**, so as to elucidate how chlorine and alkali-containing species may interact with the secondary corrosion protection of Fe-based alloys.

The results are discussed in the following sections to provide insights into what factors that determine the secondary corrosion protection of Fe-based alloys. This is achieved by addressing the following research questions:

Q1: What are the main growth mechanisms involved in the formation of a secondary corrosion protection?
Q2. What influences do alloying elements exert on the secondary corrosion protection of Fe-based alloys?
Q3. How do corrosive species influence the growth of the secondary corrosion protection?

5.1 Secondary corrosion protection of Fe-based alloys

The oxide scales formed on Fe-based alloys after breakaway have features similar to those of the multi-layered Fe-rich oxide scales formed on low-alloy steels. Thus, the protective properties of multi-layered, Fe-rich oxide scales are not only of interest with respect to classical iron-oxide-formers, such as low-alloy steels, but also for understanding the oxidation of other Fe-based alloys, such as stainless steels and FeCrAl alloys, after the onset of breakaway corrosion. This section covers the general aspects of the oxide scales formed in the secondary corrosion regime (multi-layered Fe-rich oxide scales) at intermediate temperatures (400-600 °C) on a broad range of FeCr(Al/Ni) alloys, and illustrates how the oxide growth rate of the secondary corrosion protection may vary depending on the alloy composition.

Figure 5.1 displays the gravimetric results (i.e., oxidation kinetics) for FeCr, FeCrNi, and FeCrAl model alloys, exposed for up to 48 hours at 600 °C (5% O_2 + 95% N_2) in the presence (secondary regime) and absence (primary regime) of K_2CO_3(s), as presented in **Papers I-III**. A thermobalance was used to study the secondary corrosion regime (with K_2CO_3) in order to discern differences in incubation times to breakaway. The exposures for the primary corrosion regime (no K_2CO_3) were performed in a horizontal tube furnace (24 hours). K_2CO_3(s) was used to break down the primary corrosion protection (see Eq. 2.4 in Section 2.2.2), to allow for a systematic investigation of the secondary corrosion protection without the influences of other corrosive species, such as e.g. chlorine and/or water vapour. The inserted image in Figure 5.1 displays the primary corrosion regime, for the alloys exposed in the absence of K_2CO_3. The growth rate of the secondary corrosion protection is 1-2 orders of magnitude higher than that of the primary corrosion protection. Thus, the gravimetric results clearly illustrate the two corrosion regimes before (primary regime) and after (secondary regime) the onset of breakaway corrosion.

All of the alloys studied in the secondary corrosion regime formed multi-layered Fe-rich oxide scales (see **Papers I-III**). However, the growth rates of the formed Fe-rich oxide scales varied as the alloy composition was altered (see Figure 5.1). The oxidation kinetics, in combination with the microstructural investigation (see **Papers I-III**), imply mainly diffusion-controlled growth for all the oxides investigated. The incubation times to breakaway were short for all the exposed alloys (see **Paper I**), and the measured oxide scale thicknesses were in good agreement with the calculated thicknesses based on mass gain data (for details, see **Papers I-III**). This suggests that the secondary corrosion protection formed homogeneously over the sample surface and that the oxide scale thicknesses can be used in order to compare the growth rates of the secondary corrosion protection without taking into account the incubation times to breakaway.

Note that Figure 5.1 clearly distinguishes between poor (fast-growing) and good (slow-growing) secondary corrosion protection. Thus, the Fe-based alloys can be divided into two material classes based on their performance after breakaway: those forming poorly protective oxides after breakaway, and those forming a good secondary corrosion protection. The poorly protective oxides grow at rates similar to those of low-alloy steels and pure iron exposed under dry conditions (5% O_2 + 95% N_2) (see Figure 5.1) [17, 92]. The

growth rates of the good secondary corrosion protection is approximately one order of magnitude slower than those forming poor secondary corrosion protection. Thus, the good secondary corrosion protection may be considered to act as a semi-protective barrier on Fe-based alloys exposed under conditions where the primary corrosion protection is not sustained. The following sections will discuss the main growth mechanisms that are suggested to be involved in the formation of the secondary corrosion protection, to provide insight into what factors that may determine whether an alloy will form a poor or a good secondary corrosion protection after breakaway.

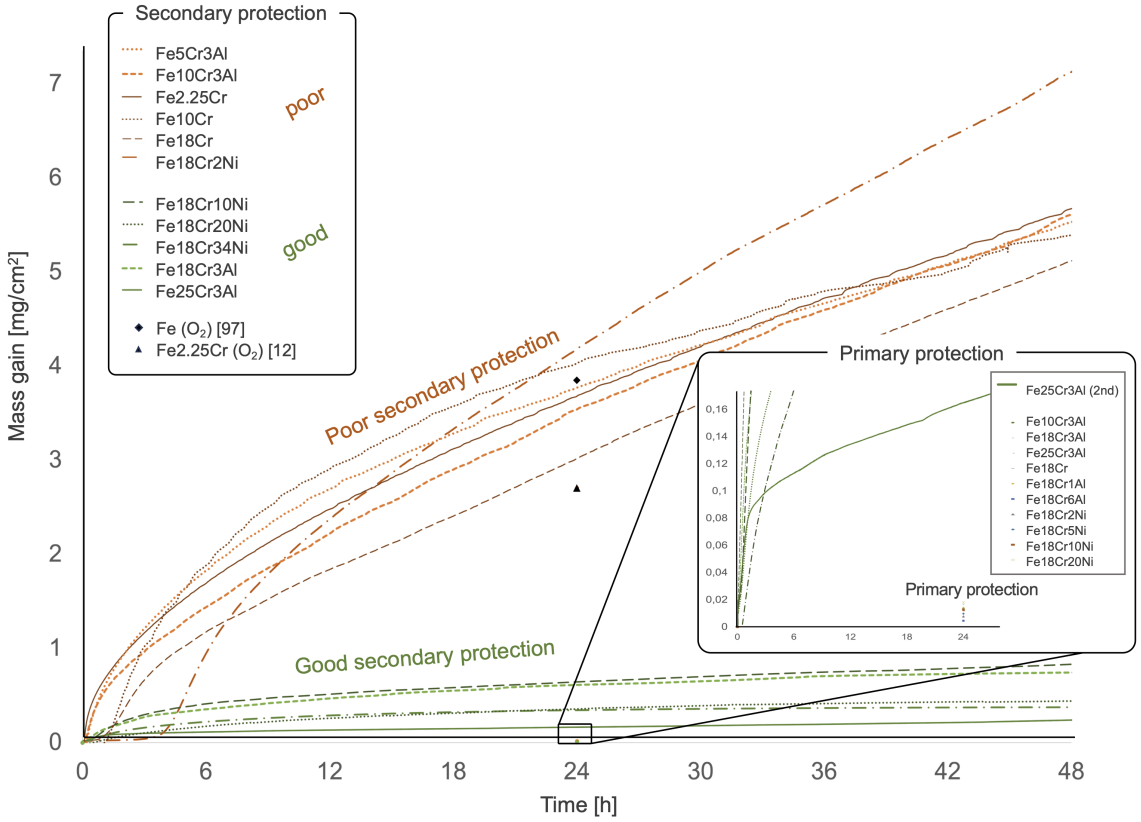

Figure 5.1: Mass gains recorded for a) FeCr, FeCrAl, and FeCrNi alloys exposed for up to 48 hours (5% O_2 + 95% N_2) at 600 °C with 1 mg/cm^2 $K_2CO_3(s)$ deposited prior to exposure to induce breakaway. The growth rates clearly demonstrate the separation into poor- and good secondary corrosion protection. The inserted image displays the primary corrosion regime. The growth rate of the secondary corrosion protection is 1-2 orders of magnitude higher than the primary corrosion protection. The mass gains recorded for Fe [92] and Fe2.25Cr [17] exposed in 5% O_2 + 95% N_2 at 600 °C are plotted for comparison.

5.2 What factors determine the secondary corrosion protection of Fe-based alloys?

To examine how a good secondary corrosion protection may be obtained it is necessary to evaluate several aspects of the formed oxide scales, as discussed in **Papers I-V**. This work aims to provide a general overview of the factors critical for predicting the secondary corrosion protection, to be used as a framework for future material development, and selection of material to be used in corrosive conditions.

Q1. What are the main growth mechanisms involved in the formation of a secondary corrosion protection?

The oxide scale formed after breakaway has previously been studied in various environments and is known to consist of a multi-layered, Fe-rich oxide scale [4,6,8,12,14,18,25,44]. A similar type of oxide scale forms on all three material systems (FeCr, FeCrAl and FeCrNi) in the secondary corrosion regime , i.e., after breakaway. The microstructural investigations and oxidation kinetics strongly suggest that the growth of the secondary corrosion protection is mainly diffusion-controlled in the studied conditions for all the Fe-based alloys investigated. The relative amounts of inward-growing and outward-growing scales remain similar (approximately 40% inward- and 60% outward-growing). This indicates that the anion and cation diffusion in the secondary corrosion protection are affected to similar extents as the alloy composition is altered.

The outward-growing oxides are similar for all the materials investigated, both regarding microstructure and chemical composition (pure Fe-oxides). Thus, from the results presented in this work (**Papers I-V**) it is suggested that the inward-growing oxide is responsible for the improved secondary corrosion protection afforded to alloys with certain compositions. A typical example of the Fe-rich oxide scale formed as the secondary corrosion protection is presented in Figure 5.2.

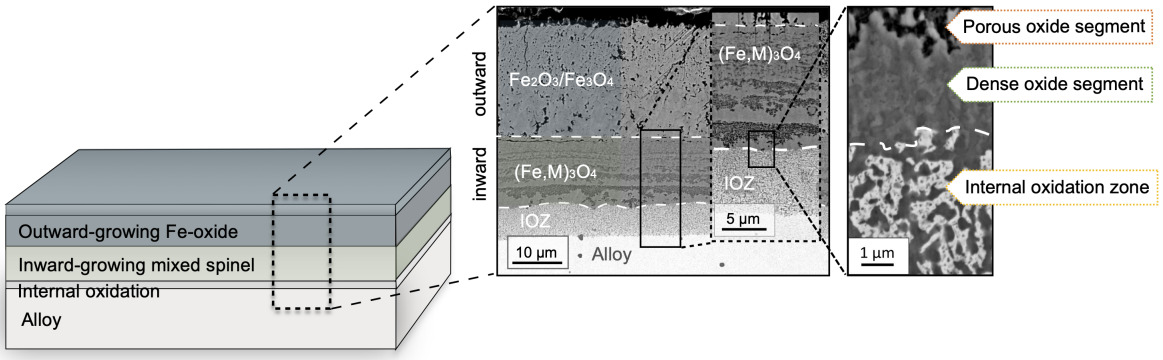

Figure 5.2: Illustration and example (BSE-SEM images) of the type of oxide scale formed as the secondary corrosion protection of Fe-based alloys at 600 °C. Note the morphology of the inward-growing scale, including dense and porous oxide segments, above the internal oxidation zone (IOZ).

The oxide scale consists of an outward-growing iron-oxide and an inward-growing mixed spinel. Internal oxidation is observed at the scale/metal interface, in agreement with the findings of previous studies [8, 18, 93]. The oxide precipitates have previously been shown to be Cr-rich spinel in a Cr-depleted alloy matrix [18, 93], in good agreement with the observations in this work (**Papers I-IV**), and the phase diagram of the FeCrO-system (see Figure 5.5). The inward-growing spinel often exhibits a banded microstructure with alternating dense and porous oxide segments (see Figure 5.2). The porous structure has previously been suggested to be remnants of the internal oxidation zone (IOZ) [18]. However, the growth mechanism, explaining the periodic nature of the inward-growing spinel is not fully understood. Based on the microstructural investigations performed in this work, it is proposed that the alterations between porous and dense oxide segments stem from the competition between rapid consumption of Fe, and Cr-replenishment in the IOZ, as illustrated in Figure 5.3.

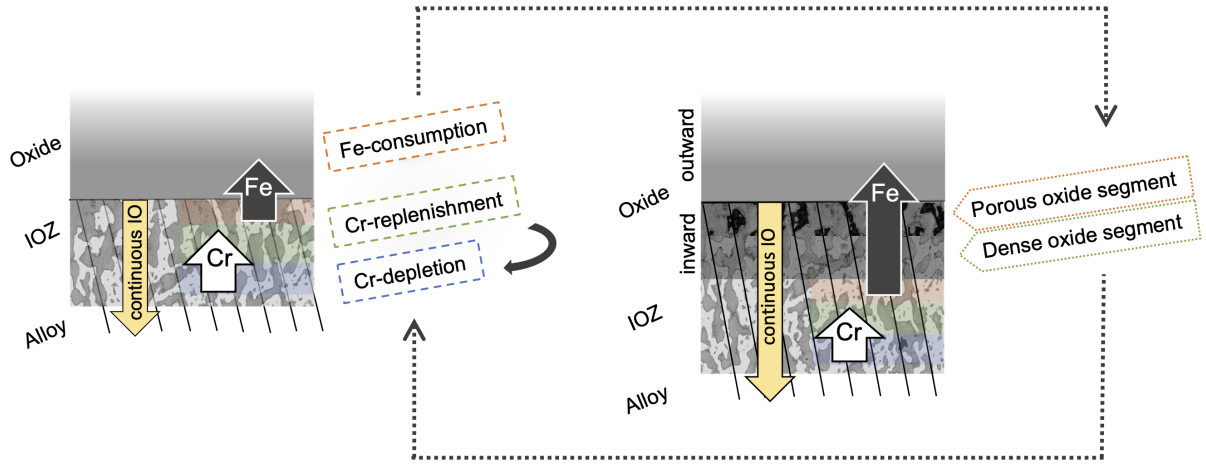

Figure 5.3: Schematic illustration of the mechanism proposed for formation of alternating dense and porous segments in the inward-growing scale. Internal oxidation results in the formation of Cr-rich spinel precipitates and Cr-depleted BCC (IOZ). The Cr-depleted BCC_{Fe} is rapidly consumed, resulting in the formation of a porous segment. The underlying region is given time to undergo replenishment with Cr, allowing for the formation of a continuous segment of Cr-rich spinel (dense segment) underneath the porous segment. The process continues periodically since the Cr-replenishment depletes the region underneath the dense segment, hindering further Cr-replenishment of the Fe-rich BCC, again resulting in rapid consumption of Fe and the formation of another porous segment.

The IOZ is composed of Cr-rich spinel precipitates in a Cr-depleted (i.e., Fe-enriched) BCC-metal. The results in **Paper IV** suggests that the Fe-rich matrix is rapidly consumed to form an outward-growing hematite, leaving behind pores at the position of the previous Fe-rich matrix. This is in good agreement with Figure 5.2, which shows that the pores have a morphology that is almost identical to that of the Fe-rich matrix (bright contrast) in the IOZ. Thus, the formation of the porous segments in Figure 5.2, is proposed to be explained by the rapid consumption of Fe-rich BCC (in the IOZ), which is used to grow the outward-growing scale.

Furthermore, the microstructural investigation in **Paper IV** shows that the dense oxide segments of the inward-growing spinel, also clearly resemble the IOZ (see insert in Figure 5.2). This indicates that the internal oxidation is active in the formation of both the dense and porous oxide segments, implying that internal oxidation is a continuous process. These observations suggests that the periodic nature of the porous bands could be kinetically explained by the competition between Fe consumption and Cr-replenishment (see Figure 5.3). During the process of Fe-consumption, the underlying segment in the IOZ is afforded sufficient time to replenish (with Cr) the Cr-depleted (i.e., Fe-rich) BCC-metal in the IOZ. This enables for the formation of a dense oxide segment, provided that there is enough Cr to form a continuous layer of Cr-rich spinel. The process may continue periodically since the Cr-replenishment depletes the region underneath the dense segment, hindering further Cr-replenishment of the underlying Fe-rich BCC. Thus, the conditions for rapid consumption of Fe-rich BCC are restored, resulting in a subsequent porous segment, as illustrated in Figure 5.3.

The amount of Cr needed to replenish an internally oxidised segment dictates the volume of Cr-depleted (i.e., Fe-rich) metal in the segment below. Therefore, the thicknesses of the porous and dense segments are coupled in that a thicker porous segment is expected to result in a thicker dense oxide segment. The frequency of the periodic alternations (between porous and dense oxide segments) decreases as the process progresses (see Figure 5.2), resulting in thicker, porous and dense oxide segments as one moves closer to the metal/oxide interface. The reduction in frequency is simply explained by the increased diffusion barrier, as the oxide grows thicker; and the coupling of the dense and porous oxide segments.

It may be noted that the inward-growing scale formed on the good secondary corrosion protection, formed on FeCrNi-alloys, also displays a periodic microstructure (see **Paper III**). However, the alterations are between fully oxidised segments, and segments rich in FCC (instead of BCC/pores). The suggested competition between Fe and Cr to explain the alternating structure is expected to valid also for this system, bu tneeds to be studied in further detail.

Q2. What influences do alloying elements exert on the secondary corrosion protection of Fe-based alloys?

Alloying elements, such as Cr, Ni and Al, are well known to improve the primary corrosion protection of Fe-based alloys (see Section 2.2.1). However, in this work, the influences of alloying elements on the FeCrNi- and FeCrAl-systems are not investigated for the primary corrosion protection (Al/Cr-rich $M2O_3$), but for the Fe-rich oxides formed on FeCrNi/Al alloys after breakaway, i.e., the secondary corrosion protection.

As shown in Figure 5.1, different alloy composition strongly influences the growth rate of the oxide scales formed also after breakaway. However, the influence of each individual alloying element is not obvious. Figure 5.4 shows a summary of the thicknesses of the multi-layered Fe-rich oxides formed on a broad range of Fe-based alloys after exposure for 48 hours at 600 °C. Figure 5.4 clearly shows that an increased amount of Cr (2.25-18 wt%) has little influence on the growth rate of the secondary corrosion protection in the binary FeCr-alloys, whereas it has a strong influence in the Fe**Cr3Al** alloys. Furthermore, the influence of Al is evident for the Fe**18Cr**Al alloys, resulting in a gradually decreasing oxide growth rate from 0-3 wt% Al. However, if the amount of Cr is not sufficient, the 3 wt% Al does not result in a slow-growing, Fe-rich oxide scale (see the Fe**Cr**3Al-alloys in Figure 5.4). The influence of Ni is also apparent, resulting in relatively slow-growing Fe-rich oxide scales for Ni contents above 2 wt%, with no significant reduction in growth rate observed as the amount of Ni is increased further. The microstructural investigations carried out in this work indicate that the outward-growing Fe-oxide scales remain similar for all alloy compositions, suggesting that the major influence of an alloying elements is to alter the growth mechanisms of the inward-growing scale.

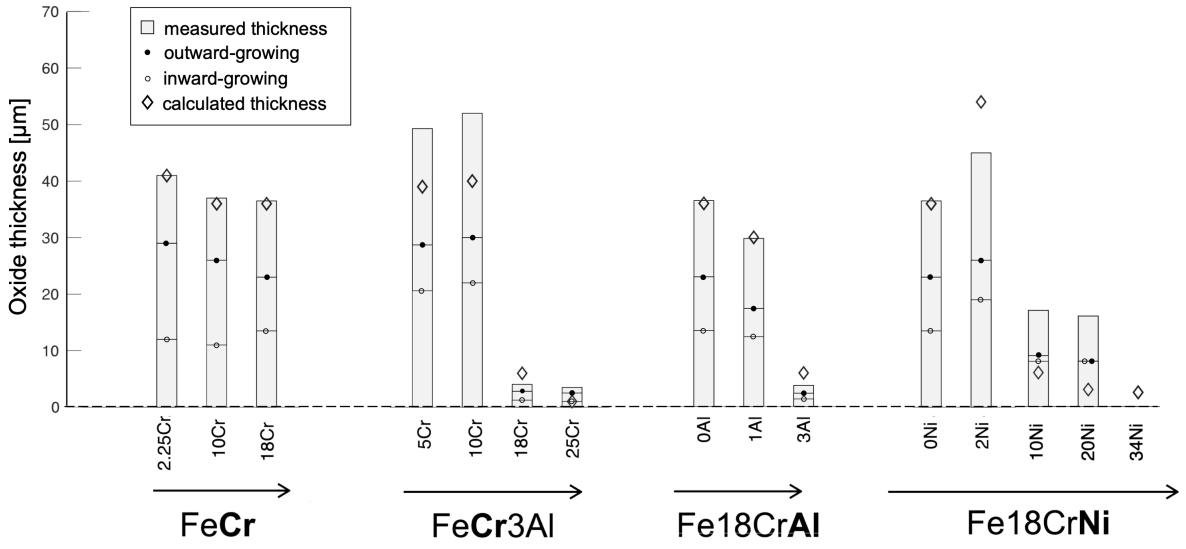

Figure 5.4: Summary of the measured oxide scale thicknesses for all model alloys exposed for 48 hours in 5% O_2 + 95% N_2 + 1 mg/cm^2 K_2CO_3(s) at 600 °C, including estimated thicknesses, calculated from mass gain data, (◇). Note that the oxide scale formed on the Fe18Cr34Ni alloy was not examined in cross section.

Detrimental internal oxidation (D-IO)

To investigate further the main growth mechanisms involved in the inward-growing scale one may examine the influences of alloying elements from a thermodynamic perspective. Since the inward-growing scale form partly through internal oxidation the influences of alloying elements can be examined by the thermodynamic stability region of internal oxidation. Thus, using thermodynamics, in combination with the chemical composition of the inward-growing spinel, provides insight into how alloying elements influence the secondary corrosion protection of Fe-based alloys (see **Papers II-V**).

The phase diagram for the FeCrO-system is shown in Figure 5.5. The phase diagram illustrates how the amounts of Cr, and the level of pO_2 (i.e., depth of the oxide scale), affect the thermodynamic stability of the different phases, as described in Section 2.1.1. The growth mechanisms proposed in Section 5.2, proposed that the rapid consumption of Fe, from the Fe-rich BCC-metal in the IOZ, is the main reason for the poor secondary corrosion protection observed on certain alloys. Thus, it is suggested that internal oxidation involving the Fe-rich BCC is the most critical factor in determining the secondary corrosion protection of Fe-based alloys (for details see **Papers II** and **III**). Hence, this type of internal oxidation is hereinafter referred to as *detrimental internal oxidation* (D-IO) and is indicated in Figure 5.5 (S_{Cr}+M), and includes Cr-rich spinel oxide (S_{Cr}) and Fe-rich metal (BCC_{Fe}). Note that the region of D-IO also involves a metallic FeNi-phase (FCC) for the FeCrNi-system (see Figure 5.6b).

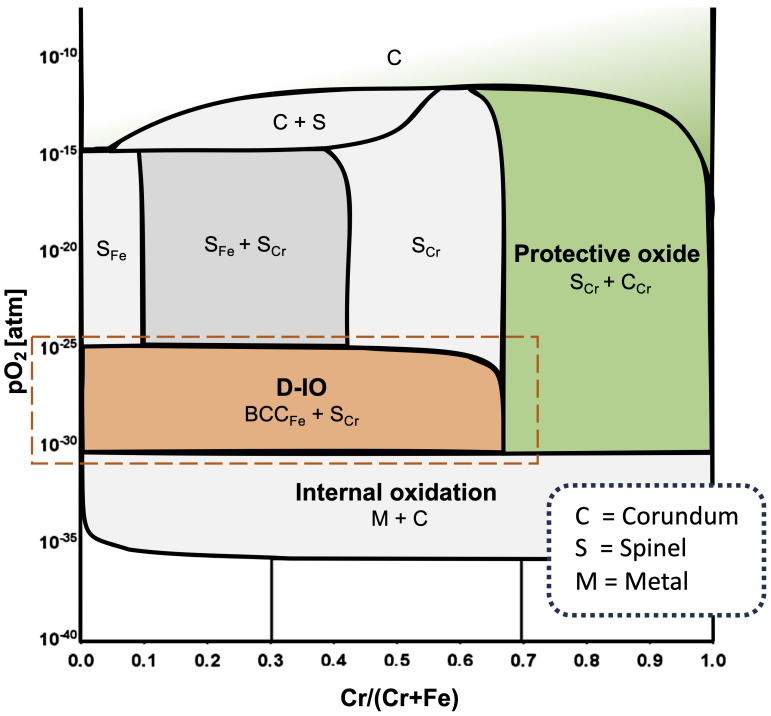

Figure 5.5: Phase diagram for the FeCrO-system, as calculated at 600 °C by H. Larsson, using the Thermo-Calc software [94] with the TCOX11 database.

The region was further examined for different amounts of Al and Ni (see Figure 5.6). As described in Section 2.1.1, the amounts of Ni and Al were set at fixed values in the calculations. By fixing the amounts of Al (or Ni) to different values, the influences exerted to the stability region of different phases may be visualised. This strategy allows for evaluation of the influences of Cr in combination with Fe, O and other alloying elements (e.g, Al or Ni). From Figure 5.6 it is obvious that the stability region of the D-IO is altered as the amounts of Al or Ni is increased. The region of D-IO (indicated in grey) is shifted to the left in the phase diagrams as the amounts of Al or Ni is increased. Thus, less Cr is required to escape the D-IO for higher Al or Ni contents (for details see **Paper II-III**). The chemical compositions of the inward-growing scales strengthen the suggestion that

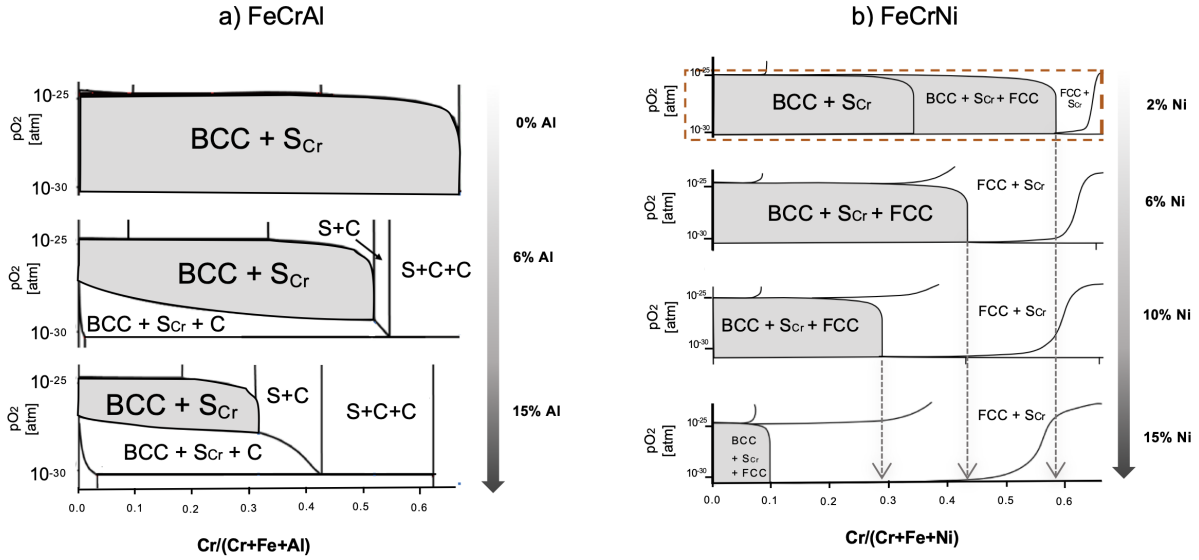

Figure 5.6: Phase diagrams showing the D-IO region, indicated in grey, for the a) FeCrAlO-system, and b) FeCrNiO-systems, at fixed amounts of Al(a) and Ni(b), as calculated at 600 °C by S. Bigdeli (a) and H. Larsson (b) using the Thermo-Calc software [94] with the TCOX10 and TCOX11 databases.

D-IO is the crucial factor for determining if the alloy will exhibit poor or good secondary corrosion protection. All alloys that exhibited poor secondary corrosion protection in this work formed inward-growing scales with an average composition that lies in the middle of the stability region for D-IO. In contrast, alloys that exhibit good secondary corrosion protection formed inward-growing scales with average compositions that lie outside of this stability region (see Figure 5.6). Thus, it is proposed that the secondary corrosion protection is mainly determined by the ability of the alloy to escape D-IO, consequently avoiding the rapid consumption of Fe from the Fe-rich BCC.

In summary, even though the corrosion process may seem complex, it is suggested that the general influences of alloying elements on the secondary corrosion protection may, to a large extent, be explained by simple thermodynamics. The thermodynamics indicate that an increased amount of Al or Ni, would reduce the amounts of Cr required to escape the detrimental internal oxidation, which is suggested to be a major factor to determine the alloys performance after breakaway.

Beyond internal oxidation

In addition to the avoidance of D-IO, the increased amount of Cr also result in that Cr-rich corundum-type oxides (C) becomes thermodynamically stable (see Figure 5.5). As described in Section 2.2, the Cr(/Al)-rich corundum type oxides represent the primary type of corrosion protection, which act as a more efficient diffusion barrier than the mixed spinel oxides. Thus, the formation of a Cr-rich, corundum-type oxide in the position of the inward-growing scale (below the Fe-oxide scale) would be expected to reduce the overall growth rate. The results obtained throughout this work indicate that a corundum-type oxide indeed may form in the inward-growing scales of the alloys that exhibit a good secondary corrosion protection (see **Papers II** and **IV**). However, the corundum-type oxide does not form a continuous healing-layer, but is instead dispersed within the Cr-rich spinel, which is in good agreement with the phase diagram in Figure 5.6. Nevertheless, the oxides classified as good secondary corrosion protection, are realtively slow-growing and the observations in this work, indicate that the good secondary corrosion protection may, given time, transition into a primary corrosion protection beneath the outward-growing Fe-oxide scale. The results are in good agreement with a long-term, time-resolved study, recently performed by Ssenteza et al. [95], in which they observed that the inward-growing spinel formed after breakaway of a FeCrNi alloy, transitioned into a corundum-type oxide after longer exposures (>1000 hrs).

Furthermore, the distribution of alloying elements within the inward-growing spinel was investigated in **Paper V** by means of atom probe tomography (APT). Figure 5.7) shows the distribution of alloying elements, as measured by APT, in the outermost part of the inward-growing oxide scales of alloys forming both poor (a:Fe10Cr4Al, c:Fe18Cr2Ni) and good (b:Fe10Cr4Al2Si, d:Fe18Cr10Ni) secondary corrosion protection. The diffusion through the outermost inward-growing scale is considered to be important for the growth propagation of the inward-growing scale. Thus, the distribution of alloying elements in this oxide region may provide insight to the secondary corrosion protection of Fe-based alloys. The elemental distributions shown in Figure 5.7) reveal distinct separations in composition for all the investigated inward-growing oxide scales. The distribution of Fe-rich spinel on the alloys that exhibit poor secondary corrosion protection indicates a continuous network, in the oxide growth direction, in contrast to the alloys exhibiting good secondary corrosion protection. It is reasonable to assume that a continuous network of Fe-rich spinel in the growth direction would influence the diffusion through the inward-growing scale. Thus, the indicated continuous network of Fe-rich spinel may serve as an additional rapid diffusion pathway in alloys exhibiting poor secondary corrosion protection. However, since the analysed volumes in APT analysis are small, further studies are required to make further conclusions.

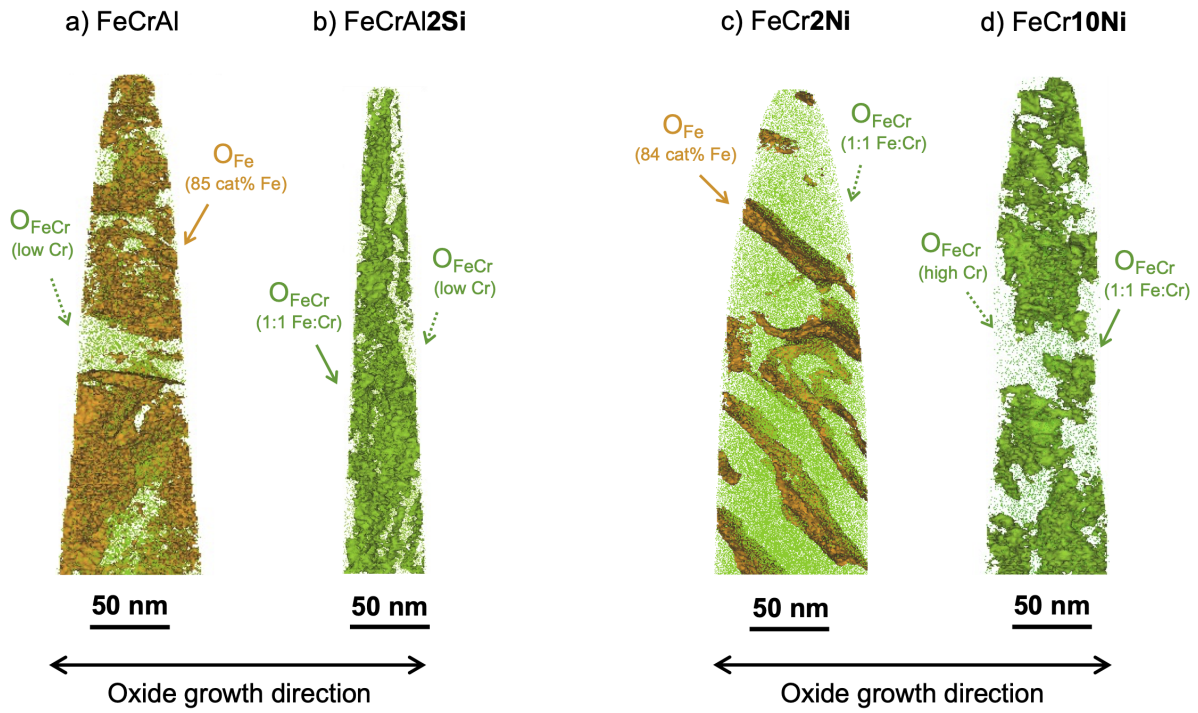

Figure 5.7: Distribution of alloying elements (as measured by APT) in the inward-growing oxide formed on alloys exhibiting poor (Fe10Cr4Al, Fe18Cr2Ni), and good (Fe10Cr4Al2Si, Fe18Cr10Ni) secondary corrosion protection. The orange isosurfaces illustrate the continuous network of Fe-rich (FeCrAl/Ni) spinel formed on the poorly protective oxides (a+c), whereas the green isosurface illustrate the distribution of FeCrAl/Ni spinel with an Fe:Cr relation of 1:1 (O_{Cr}(1:1,Fe:Cr)) as formed on the alloys exhibiting good secondary corrosion protection (b+d) (for details on oxide composition, see **Paper V***).*

Q3. How do corrosive species influence the growth of the secondary corrosion protection?

Chlorine- and alkali-containing species are well known to accelerate the corrosion of Fe-based alloys, including low-alloyed steels [27, 63, 64, 67, 69, 70, 72, 77–83], stainless steels and FeCrAl alloys [8, 23–25, 27, 44, 46–51, 63, 64, 66–70, 72, 73, 75, 76, 96]. The proposed corrosion mechanisms are numerous and are typically focused on how these species induce breakdown of the primary corrosion protection, or how the presence of chlorine-containing species accelerates the corrosion process through chemical reactions, such as, for example, the proposed active oxidation mechanism [45, 67].

In this thesis, the influence of alkali- and chlorine containing species are discussed regarding how its presence may change the microstructure and growth rates of the multi-layered Fe-rich oxide scales. This is in order to to better understand how it may change the capability of the Fe-rich oxide to withstand further corrosion. **Papers IV-VII** investigates how different alkali- and chlorine-containing species (KCl, HCl) influence the microstructure of the multi-layered Fe-rich oxide scales. **Papers IV-V** studies the oxides formed on FeCrAl and FeCrNi model alloys exposed at 600 °C, whereas **Papers VI-VII** investigates the oxide formed on a commercial low-alloyed steel (Fe2.25Cr1Mo) exposed at 400 °C. Note that the oxide scale formed on low-alloyed steels are of only one type (secondary type). Thus, its properties in various environments may be used to increase our understanding as to how corrosive species may affect the secondary corrosion protection also on FeCrNi/Al alloys.

The results in this thesis clearly demonstrate that the presence of alkali- and/or chlorine containing species, has a great influence on both the growth rate and microstructure of the multi-layered Fe-rich oxide scales (see **Papers IV-VII**). Figure 5.8 illustrates how the presence of KCl may influence the growth rate of the oxide formed on a low-alloyed steel exposed at 400 °C. The growth kinetics indicate diffusion controlled growth (parabolic kinetics) both in the absence (reference) and presence of KCl. However, the parabolic rate constant is greatly affected by the presence of KCl, indicating that the diffusion through the oxide scale has been significantly altered by the presence of KCl.

Moreover, the presence of KCl induces a kinetic transition (see Figure 5.8), explained by the delamination of the oxide scale in combination with the formation of cracks (for details see **Paper VI**). This indicates that the presence of KCl may influence the integrity and adherence of the oxide scale, being at high risk for oxide spallation. Oxide spallation is of major concern for many applications, since loss of the oxide scale and consequent recurring oxide growth, result in high corrosion rates. Thus, the overall corrosion rate becomes the sum of the oxides grown between the spallation events. Hence, the loss in integrity/adherence in combination with the accelerated, diffusion-controlled, oxidation are both important factors when considering the influence of chlorine containing species on the secondary corrosion protection.

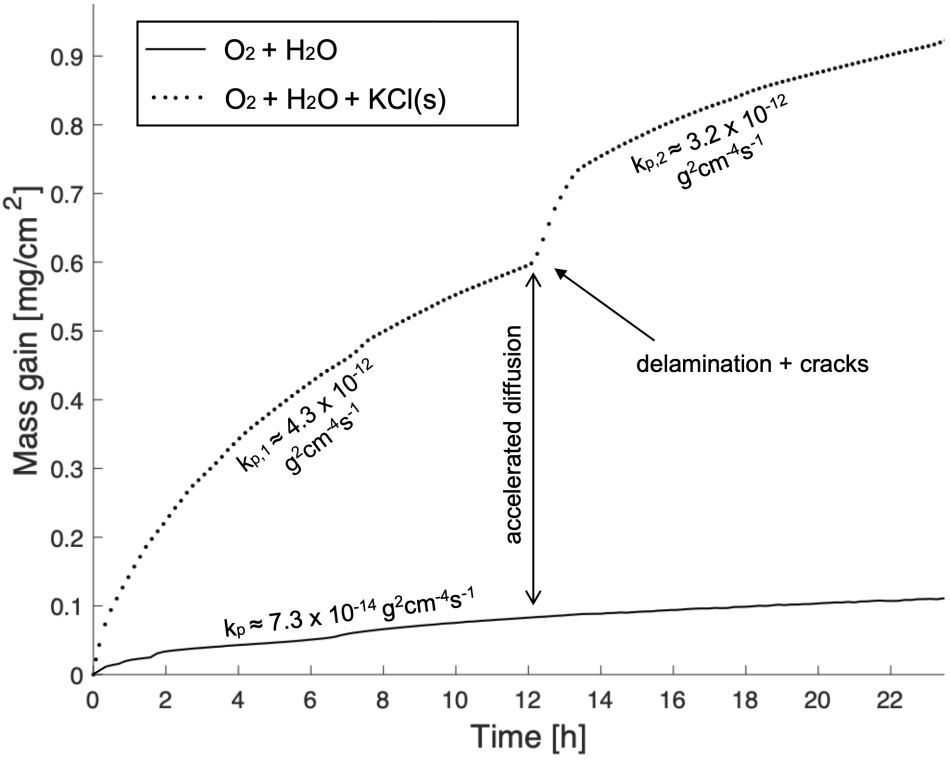

Figure 5.8: Thermogravimetric analysis showing the oxidation kinetics of Fe-2.25Cr-1Mo exposed at 400 °C in 5% O_2 + 20% H_2O + 75% N_2 in the absence (reference) and presence of 0.1 mg/cm^2 KCl(s). Both curves are parabolic, with different parabolic rate constants. A kinetic transition is observed in the presence of KCl(s), with similar parabolic rate constants before and after the transition.

Furthermore, the results in **Papers IV** suggests that the presence of KCl and H_2O, significantly altered the microstructure of the inward-growing scale formed on a Fe10Cr3Al model alloy (see Figure 5.9). The inward-growing scales formed on FeCrAl alloys are suggested to involve internal oxidation and rapid consumption of Fe, leading to a microstructure composed of alternating porous and dense oxide segments upon exposure to e.g., K_2CO_3 (see Section 5.2). However, the microstructural investigation performed in **Paper IV** demonstrates that the porous microstructure of the inward-growing scale formed in the presence of KCl exhibit a microstructure with pores distributed throughout the entire inward-growing scale 5.9), in contrasst to the exposure to K_2CO_3.
Building upon the proposed competition between Fe-consumption and Cr-replenishment, suggested in Section 5.2, the absence of dense oxide segments in the presence of KCl+H_2O, implies that the Cr-replenishment of the IOZ is affected by the presence of KCl and/or H_2O. The replenishment of Cr could be hindered by either retarding the diffusion of Cr in the alloy (slowing down the Cr-replenishment) or by accelerating the outward-diffusion of Fe, as illustrated in Figure 5.9. It is reasonable to assume that any mechanisms that results in accelerated oxide growth rates will increase the outward-diffusion of Fe-ions (since the outward-growing oxide scale grows faster). It is difficult to determine whether the accelerated outward-diffusion is caused by the presence of H_2O, KCl or a combined effect, since both these variables changed between the two exposures (KCl and K_2CO_3), see **Paper IV**. Regardless, the fully porous oxide scale, formed in the presence of KCl (and

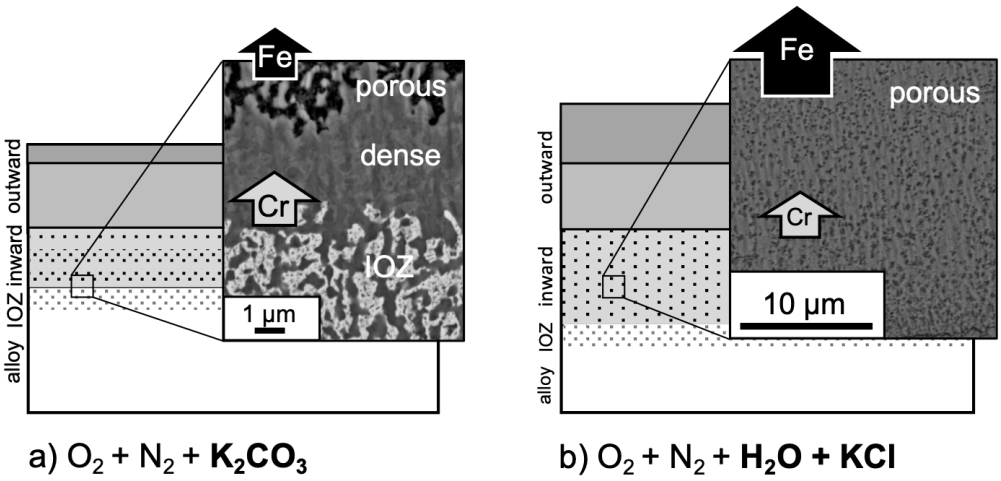

Figure 5.9: Schematics (and SEM-BSE images) illustrating the difference in microstructure of the inward-growing scale formed on a Fe10CrAl alloy after exposure for 2000 hrs at 600 °C in a) O_2+N_2 + K_2CO_3(s), and b) O_2+H_2O+N_2 + KCl(s), indicating that the IOZ is not sufficiently replenished with Cr to form the dense oxide segment in the presence of KCl (and H_2O).

H_2O), is suggested to be explained by the accelerated outward-diffusion of Fe through the spinel. Thus, this observation makes it tempting to speculate and elaborate on possible pathways for KCl and H_2O to influence the outward-diffusion of Fe in the spinel.

The presence of water vapour has previously been shown to accelerate the growth rate of iron oxide and has been suggested to influence the grain boundary transport in the hematite layer [17, 92, 97]. This is in line with the observations in **Paper IV**, where a thicker hematite layer was observed to form in the presence of KCl and H_2O. However, the results in **Paper IV** imply that the increased amount of hematite is closely linked to the increased amount of pores in the inward growing scale. Thus, this suggests that the outward-diffusion through the spinel, at least for this particular system, is rather related to the transport properties of Fe in the inward-growing scale.

One possible pathway to accelerate the diffusion of Fe through the spinel oxide could be through the reduction of Fe^{3+} to Fe^{2+}, since divalent ions in general diffuse more rapidly than trivalent ions in an Fe-rich spinel [36]. Another pathway could be to change the distribution of Fe-ions between tetrahedral and octahedral lattice sites, since it has been suggested to be easier for Fe^{2+} to diffuse from an octahedral position in the spinel than from a tetrahedral position [98]. Thus, one could speculate that the role of KCl and/or H_2O is to either enable the reduction of Fe in the spinel oxide or to enforce Fe-ions to be positioned in octahedral lattice sites. Note that these pathways are only speculative and that the results included in this thesis are not sufficient to make any conclusions regarding these two pathways. However, the results in this work clearly indicate that the influence of KCl (and/or H_2O) is in some way related to the increased diffusion of iron in the inward-growing scale.

6

Summary & Outlook

The corrosion protection of stainless steels and FeCrAl alloys often rely on the formation of a slow-growing, Cr- and/or Al-rich, corundum-type oxide scale. However, in corrosive environments, these oxide scales tend to break down, resulting in the formation of a fast-growing, multi-layered, Fe-rich oxide scale, a well-known process referred to as *breakaway corrosion*. The Fe-rich oxide scales formed after breakaway have features similar to the oxides formed on low-alloyed steels and are often considered to be non-protective. Nevertheless, in many industrial application, breakaway corrosion may be difficult to prevent. Thus, the corrosion propagation and lifetime of metallic components exposed to corrosive conditions are often determined by the protection of the Fe-rich oxide scale formed after breakaway.

Previous studies on the breakaway corrosion of Fe-based alloys have mainly focused on how to delay, or prevent, the breakdown of the Cr/Al-rich oxide. However, this work clearly demonstrate that the protection of the Fe-rich oxide scales formed on stainless steels and FeCrAl alloys after breakaway may be significantly improved at intermediate temperatures (400-600 °C). Therefore, in this work, the event of breakaway corrosion is not treated as a stage of failure, but rather as a transition from one type of corrosion regime, **the primary corrosion regime** (before breakaway), to another, **the secondary corrosion regime** (after breakaway).

This thesis provides a general overview of the factors critical for predicting the secondary corrosion protection of Fe-based alloy at intermediate temperatures (400-600 °C). This information may be used as a framework for material development, selection of materials for harsh environments, and future research of the secondary corrosion regime for longer exposure times. The protective properties of the multi-layered Fe-rich oxides formed after breakaway, i.e., the secondary corrosion protection, are studied through a combination of advanced microscopy and thermodynamic equilibrium calculations. This strategy made it possible to investigate the influences of alloying elements (Cr, Al, Ni and Si) on the secondary corrosion protection. By inducing rapid breakdown of the normally formed Cr-/Al-rich M_2O_3, i.e., the primary corrosion protection, on several sets of model alloys (FeCr, FeCrAl, FeCrNi), the secondary corrosion protection could be investigated systematically. The focus of the investigations have been set to how alloying elements, and the presence of corrosive species, influences the protective properties of the Fe-rich oxide scales formed after breakaway. The results were discussed addressing a number of key research questions (Q1-Q3), which will be summarised below.

Q1: What are the main growth mechanisms involved in the formation of a secondary corrosion protection?
The secondary corrosion protection is shown to be mainly diffusion-controlled under the investigated conditions and may be improved by alloying with certain combinations of elements. The influences that alloying elements exert on the Fe-rich oxide scales are shown to be different from the previously demonstrated effects of the slow-growing Cr/Al-rich corundum-type oxides.

The fact that the secondary corrosion protection is shown to be mainly diffusion-controlled, enables for the use of diffusion-based modelling tools to predict the corrosion behaviour in harsh environments. The similarities in growth rates and microstructure between poor secondary corrosion protection and oxidation of pure iron, as observed in this work, suggest that the poor secondary corrosion protection could be modelled as a pure iron oxide. This enables for simplified lifetime predictions for a wide range of Fe-based alloys by available diffusion-based modelling tools, such as DICTRA [94]. In a diffusion-controlled regime it may in addition be possible to alloy for a more protective secondary protection, see below.

Q2. What influences do alloying elements exert on the secondary corrosion protection of Fe-based alloys?
The results in this work imply that Fe-based alloys can be divided into two material classes determined by their performance after breakaway: those forming poorly protective Fe-rich oxides after breakaway, and those forming a good Fe-rich secondary corrosion protection. The poorly protective oxides are shown to grow at similar rates as pure iron, whereas the good secondary corrosion protection grow significantly slower (approximately one order of magnitude difference). This is mainly explained by the ability for certain alloys to escape internal oxidation containing Fe-rich BCC-metal and Cr-rich spinel oxide, i.e., detrimental internal oxidation (D-IO). It is suggested that the onset of D-IO result in rapid consumption of iron, from the Fe-rich BCC, explaining the growth rates of the poor secondary corrosion protection and the porous microstructure observed. Thus, the corrosion protection after breakaway may be improved by the addition of Cr and sufficient amounts of Al or Ni, shifting the thermodynamic stability region for D-IO. The aspect of the shifted stability region for D-IO, as a factor for determining if the alloys exhibit poor- or good secondary corrosion protection, could be used in material development and selection of materials to be used in corrosive conditions.

Q3. How do corrosive species influence the growth of the secondary corrosion protection?
The results presented in this thesis imply that the growth of the Fe-rich oxide scales remain diffusion-controlled also in the presence of potassium- and chlorine-containing species. However, the presence of chlorine containing species is observed to influence the growth of the Fe-rich oxide scale in two ways. First, the growth rates of the Fe-rich oxide scales are observed to be accelerated in the presence of KCl (and H_2O/HCl), suggested to be explained by increased diffusion of Fe thorough the spinel oxide. Second, the presence of KCl is observed to sometimes result in cracks and delaminated oxide scales, suggesting a reduction in oxide integrity, and/or adherence (i.e., high risk for oxide spallation). In many applications, the material lifetime is determined by the sum of material lost to corrosion

between recurring spallation events. Thus, the loss in integrity/adherence in combination with the accelerated, diffusion-controlled, oxidation are both important factors when considering the influence of chlorine containing species on the secondary corrosion protection.

Moreover, the observations in this thesis indicate that the good secondary corrosion protection may, given time, transition into a primary corrosion protection (Cr-rich M_2O_3) below the outward-growing Fe-oxide scale. The formation of such a slow-growing oxide, below a cap-layer of Fe-oxide. This could reduce the risk for future breakaway events induced by chemical reactions involving Cr. Hence, in corrosive conditions, where the primary corrosion protection is expected to chemically break down, it may be sensible to choose a material that form a good secondary corrosion protection, as opposed to a good primary corrosion protection. Thus, from the perspective of material development of Fe-based alloys, the secondary corrosion protection may be considered an important material property for applications operated in corrosive environments.

Acknowledgements

First of all, I would like to thank my main supervisor Torbjörn Jonsson for always being supportive and responsive for my needs. Thank you for trusting in me and for giving me the freedom to become an independent researcher. I am sincerely grateful. This journey would not have been the same without you.

I would also like to thank my co-supervisors Jesper Liske and Jan-Erik Svensson, as well as Lars-Gunnar Johansson, for their great support and interesting discussions.

Moreover, I would like to acknowledge Chalmers Materials Analysis Laboratory (CMAL) for providing excellent support and the possibility to perform versatile materials characterisation. Special thanks to staff members Stefan Gustafsson and Ludvig de Knoop.

Furthermore, I am grateful to all the PhD students, post-docs and diploma workers who have helped in providing samples and complementary data for the studies described in this thesis.

I want to thank all my present and previous colleagues in the unit of Environmental Inorganic Chemistry for providing a fun and inspiring work environment. Special thanks to Johan Eklund, Maria Dolores Paz Olausson, Mercedez Andrea Olivas Ogaz and Sandra Nayeri. I would also like to thank Christine Geers and Itai Panas for many inspiring discussions.

Last, but not least I want to thank my family and beloved children, Frans and Elis, for all the love and support. Thank you for putting things in perspective.

Amanda Persdotter, Gothenburg, 10 2023

Bibliography

[1] P. Kofstad, *High Temperature corrosion.* Elsevier Applied Science, 1988.

[2] N. Birks, G. H. Meier, and F. S. Pettit, *Introduction to the high-temperature oxidation of metals.* Cambridge University Press, 2006.

[3] D. J. Young, *High Temperature Oxidation and Corrosion of Metals (Second Edition).* Elsevier, 2016.

[4] G. C. Wood and D. P. Whittle, "The mechanism of breakthrough of protective chromium oxide scales on Fe-Cr alloys," *Corrosion science*, vol. 7, no. 11, 1967.

[5] F. Stott, G. Wood, and J. Stringer, "The influence of alloying elements on the development and maintenance of protective scales," *Oxidation of metals*, vol. 44, pp. 113–145, 1995.

[6] T. Gheno, D. Monceau, and D. J. Young, "Mechanism of breakaway oxidation of Fe – Cr and Fe – Cr – Ni alloys in dry and wet carbon dioxide," *Corrosion Science*, vol. 64, pp. 222–233, 2012.

[7] J. Pettersson, J.-E. Svensson, and L.-G. Johansson, "Alkali induced corrosion of 304-type austenitic stainless steel at 600 °C; comparison between KCl, K_2CO_3 and K_2SO_4," *Materials Science Forum*, vol. 595-598 PA, pp. 367–375, 2008.

[8] T. Jonsson, S. Karlsson, H. Hooshyar, M. Sattari, J. Liske, J.-E. Svensson, and L.-G. Johansson, "Oxidation After Breakdown of the Chromium-Rich Scale on Stainless Steels at High Temperature : Internal Oxidation," *Oxidation of metals*, vol. 85, pp. 509–536, 2016.

[9] A. Col, V. Parry, and C. Pascal, "Oxidation of a Fe–18Cr–8Ni austenitic stainless steel at 850 °C in O_2: Microstructure evolution during breakaway oxidation," *Corrosion Science*, vol. 114, pp. 17–27, 2017.

[10] H. Asteman, J. Svensson, M. Norell, and L. Johansson, "Influence of Water Vapor and Flow Rate on the High-Temperature Oxidation of 304L ; Effect of Chromium Oxide Hydroxide Evaporation," *Oxidation of Metals*, vol. 54, no. 1-2, pp. 11–26, 2000.

[11] H. Asteman, K. Segerdahl, J. E. Svensson, and L. G. Johansson, "The influence of water vapor on the corrosion of chromia-forming steels," *Materials Science Forum*, vol. 369-372, no. I, pp. 277–286, 2001.

[12] R. Peraldi and B. A. Pint, "Effect of Cr and Ni Contents on the Oxidation Behavior of Ferritic and Austenitic Model Alloys in Air with Water Vapor," *Oxidation of Metals*, vol. 61, no. 5-6, pp. 463–483, 2004.

[13] F. Liu, J. E. Tang, T. Jonsson, S. Canovic, K. Segerdahl, J. E. Svensson, and M. Halvarsson, "Microstructural investigation of protective and non-protective oxides on 11% chromium steel," *Oxidation of Metals*, vol. 66, no. 5-6, pp. 295–319, 2006.

[14] L. Liu, Z.-G. Yang, M. Zhang, K. Kawamura, and T. Maryama, "Effect of water vapour on the oxidation of Fe-13Cr-5Ni martensitic alloy at 973 K," *Corrosion science*, vol. 60, pp. 90–97, 2012.

[15] J. Ehlers, D. J. Young, E. J. Smaardijk, A. K. Tyagi, H. J. Penkalla, L. Singheiser, and W. J. Quadakkers, "Enhanced oxidation of the 9%Cr steel P91 in water vapour containing environments," *Corrosion Science*, vol. 48, no. 11, pp. 3428–3454, 2006.

[16] T. Jonsson, F. Liu, S. Canovic, H. Asteman, J.-E. Svensson, L.-G. Johansson, and M. Halvarsson, "Influence of H_2O(g) on the Oxide Microstructure of the Stainless Steel 353MA at 900 °C in Oxygen," *Journal of The Electrochemical Society*, vol. 154, no. 11, p. C603, 2007.

[17] B. Pujilaksono, T. Jonsson, H. Heidari, M. Halvarsson, J. E. Svensson, and L. G. Johansson, "Oxidation of binary FeCr alloys (Fe-2.25Cr, Fe-10Cr, Fe-18Cr and Fe-25Cr) in O_2 and in O_2 + H_2O environment at 600 °C," *Oxidation of Metals*, vol. 75, no. 3-4, pp. 183–207, 2011.

[18] T. Jonsson, B. Pujilaksono, H. Heidari, Liu F., J.-E. Svensson, M. Halvarsson, and L.-G. Johansson, "Oxidation of Fe-10Cr in O_2 and in O_2+H_2O environment at 600 °C: A microstructural investigation," *Corrosion science*, vol. 75, pp. 326–336, 2013.

[19] N. K. Othman, J. Zhang, and D. J. Young, "Water vapour effects on Fe-Cr alloy oxidation," *Oxidation of Metals*, vol. 73, no. 1-2, pp. 337–352, 2010.

[20] A. N. Hansson, K. Pantleon, F. B. Grumsen, and M. A. Somers, "Microstructure evolution during steam oxidation of a Nb stabilized austenitic stainless steel," *Oxidation of Metals*, vol. 73, no. 1-2, pp. 289–309, 2010.

[21] E. Essuman, G. H. Meier, J. Zurek, M. Hänsel, L. Singheiser, and W. J. Quadakkers, "Enhanced internal oxidation as trigger for breakaway oxidation of Fe-Cr alloys in gases containing water vapor," *Scripta Materialia*, vol. 57, no. 9, pp. 845–848, 2007.

[22] N. Mu, K. Y. Jung, N. M. Yanar, G. H. Meier, F. S. Pettit, and G. R. Holcomb, "Water vapor effects on the oxidation behavior of Fe-Cr and Ni-Cr alloys in atmospheres relevant to oxy-fuel combustion," *Oxidation of Metals*, vol. 78, no. 3-4, pp. 221–237, 2012.

[23] T. Jonsson, J. Froitzheim, J. Pettersson, J. E. Svensson, L. G. Johansson, and M. Halvarsson, "The influence of KCl on the corrosion of an Austenitic stainless steel (304L) in oxidizing humid conditions at 600 °C: A microstructural study," *Oxidation of Metals*, vol. 72, no. 3-4, pp. 213–239, 2009.

[24] C. Pettersson, L. G. Johansson, and J. E. Svensson, "The Influence of Small Amounts of KCl(s) on the Initial Stages of the Corrosion of Alloy Sanicro 28 at 600 degrees C," *Oxidation of Metals*, vol. 70, no. 5-6, pp. 241–256, 2008.

[25] T. Jonsson, H. Larsson, S. Karlsson, H. Hooshyar, M. Sattari, J. Liske, J. E. Svensson, and L. G. Johansson, "High-Temperature Oxidation of FeCr(Ni) Alloys: The Behaviour After Breakaway," *Oxidation of Metals*, vol. 87, no. 3-4, pp. 333–341, 2017.

[26] H. P. Nielsen, F. J. Frandsen, K. Dam-Johansen, and L. L. Baxter, "The implications of chlorine-associated corrosion on the operation of biomass-fired boilers," *Progress in Energy and Combustion Science 26*, pp. 283–298, 2000.

[27] M. Spiegel, A. Zahs, and H. J. Grabke, "Fundamental aspects of chlorine induced corrosion in power plants," *Materials at High Temperatures*, vol. 20, no. 2, pp. 153–159, 2003.

[28] M. Montgomery, A. Karlsson, and O. H. Larsen, "Field test corrosion experiments in Denmark with biomass fuels. Part 1: Straw-firing," *Materials and Corrosion*, vol. 53, no. 2, pp. 121–131, 2002.

[29] F. J. Frandsen, "Utilizing biomass and waste for power production - A decade of contributing to the understanding, interpretation and analysis of deposits and corrosion products," *Fuel*, vol. 84, no. 10, pp. 1277–1294, 2005.

[30] P. Henderson, P. Szakalos, R. Pettersson, C. Andersson, and J. Hogberg, "Reducing superheater corrosion in wood-fired boilers," *Materials and Corrosion*, vol. 57, no. 2, pp. 128–134, 2006.

[31] A. Syed, N. Simms, and J. Oakey, "Fireside corrosion of superheaters: Effects of air and oxy-firing of coal and biomass," *Fuel 101*, pp. 62–73, 2012.

[32] L. Paz, T. Jonsson, and J. Liske, "Testing of new materials to combat superheater corrosion in a waste fired CFB boiler," in *23rd International conference on Fluidized Bed Conversion*, 2018.

[33] S. C. Okoro, M. Montgomery, F. J. Frandsen, and K. Pantleon, "Influence of Preoxidation on High-Temperature Corrosion of a FeCrAl Alloy Under Conditions Relevant to Biomass Firing," *Oxidation of Metals*, vol. 89, no. 1-2, pp. 99–122, 2018.

[34] J. Eklund, M. D. Paz, B. Jönsson, J. Liske, J. E. Svensson, and T. Jonsson, "Field exposure of FeCrAl model alloys in a waste-fired boiler at 600 °C: The influence of Cr and Si on the corrosion behaviour," *Materials and Corrosion*, vol. 70, no. 8, pp. 1476–1485, 2019.

[35] I. Kaur and W. Gust, *Fundamentals of grain and interface boundary diffusion.* Stuttgart: Ziegler press, 1989.

[36] J. A. V. Orman and K. L. Crispin, "Diffusion in Oxides," *Reviews in Mineralogy and Geochemistry*, vol. 72, pp. 757–825, 2010.

[37] J. Topfer, S. Aggarwal, and R. Dieckmann, "Point defects and cation tracer diffusion in $(Cr_x,Fe_{1-x})_{3-\delta}O_4$ spinels," *Solid State Ionics*, vol. 81, no. 2738, pp. 251–266, 1995.

[38] R. Dieckmann, M. R. Hilton, and T. O. Mason, "Defects and Cation Diffusion in Magnetite (Viii): Migration Enthalpies for Iron and Impurity Cations." *Berichte der Bunsengesellschaft/Physical Chemistry Chemical Physics*, vol. 91, no. 1, pp. 59–66, 1987.

[39] V. Tammann, "Uber anlauffarben von metallen," *Z. Anorg. Allg. Chem.*, vol. 111, 1920.

[40] C. Wagner, "Beitrag zur theorie des anlaufvorgangs," *Zeitschrift für physicalische chemie*, vol. 21, no. 1, pp. 25–41, 1933.

[41] F. Stott, "The oxidation of alumina-forming alloys," in *High Temperature Corrosion and Protection of Materials 4*, ser. Materials Science Forum, vol. 251. Trans Tech Publications Ltd, 10 1997, pp. 19–32.

[42] H. Josefsson, F. Liu, J. Svensson, M. Halvarsson, and L. Johansson, "Oxidation of FeCrAl alloys at 500-900 °C in dry O_2," *Materials and Corrosion*, vol. 56, no. 11, pp. 801–805, 2005.

[43] M. G. Hobby, "The Role of Nickel in the High-Temperature Oxidation of Fe-Cr-Ni Alloys in Oxygen," *Oxidation of Metals*, vol. 1, no. 1, pp. 23–54, 1969.

[44] J. Eklund, B. Jönsson, A. Persdotter, J. Liske, J. Svensson, and T. Jonsson, "The influence of silicon on the corrosion properties of FeCrAl model alloys in oxidizing environments at 600 °C," *Corrosion Science*, vol. 144, pp. 266–276, 2018.

[45] M. J. McNallan, W. W. Liang, S. H. Kim, and C. T. Kang, "Accelleration of the High Temperature Oxidation of Metals by Chlorine," *High Temperature Corrosion, NACE*, pp. 316–321, 1983.

[46] J. Pettersson, H. Asteman, J. E. Svensson, and L. G. Johansson, "KCl induced corrosion of a 304-type austenitic stainless steel at 600 degrees C; The role of potassium," *Oxidation of Metals*, vol. 64, no. 1-2, pp. 23–41, 2005.

[47] J. Pettersson, N. Folkeson, L.-G. Johansson, and J.-E. Svensson, "The effects of KCl, K_2SO_4 and K_2CO_3 on the high temperature corrosion of a 304-type austenitic stainless steel," *Oxidation of metals*, vol. 76, pp. 93–109, 2011.

[48] J. Lehmusto, B.-J. Skrifvars, P. Yrjas, and M. Hupa, "Comparison of potassium chloride and potassium carbonate with respect to their tendency to cause high temperature corrosion of stainless 304L steel," *Fuel Processing Technology*, vol. 105, pp. 98–105, 2013.

[49] S. Karlsson, J. Liske, L.-G. Johansson, and J.-E. Svensson, "Alkali induced high temperature corrosion of stainless steel: the influence of NaCl, KCl and $CaCl_2$," *Oxidation of metals*, vol. 78, pp. 83–172, 2012.

[50] N. Israelsson, K. A. Unocic, K. Hellström, T. Jonsson, M. Norell, J. E. Svensson, and L. G. Johansson, "A Microstructural and Kinetic Investigation of the KCl-Induced Corrosion of an FeCrAl Alloy at 600 °C," *Oxidation of Metals*, vol. 84, no. 1-2, pp. 105–127, 2015.

[51] N. Israelsson, K. Unocic, K. Hellström, J.-E. Svensson, and L. G. Johansson, "Cyclic Corrosion and Chlorination of an FeCrAl Alloy in the Presence of KCl," *Oxidation of Metals*, vol. 84, no. 1-2, p. 269–290, 2015.

[52] H. Asteman, J.-E. Svensson, and L.-G. Johansson, "Evidence for chromium evaporation influencing the oxidation of 304L: The effect of temperature and flow rate," *Oxidation of Metals*, vol. 57, no. 3-4, pp. 193–216, 2002.

[53] B. B. Ebbinghaus, "Thermodynamics of gas phase chromium species: the chromium chlorides, oxychlorides, fluorides, oxyfluorides, hydroxides, oxyhydroxides, mixed oxyfluorochlorohydroxides, and volatility calculations in waste incineration processes," *Combustion and Flame*, vol. 93, pp. 119–137, 1993.

[54] E. J. Opila, D. L. Myers, N. S. Jacobson, I. M. Nielsen, D. F. Johnson, J. K. Olminsky, and M. D. Allendor, "Theoretical and experimental investigation of the thermochemistry of $CrO_2(OH)_2(g)$," *Journal of Physical Chemistry A*, vol. 111, no. 10, pp. 1971–1980, 2007.

[55] H. Asteman, J. E. Svensson, L. G. Johansson, and M. Norell, "Indication of chromium oxide hydroxide evaporation during oxidation of 304L at 873 K in the presence of 10% water vapor," *Oxidation of Metals*, vol. 52, no. 1, pp. 95–111, 1999.

[56] R. Y. Chen and W. Y. D. Yuen, "Review of the High-Temperature Oxidation of Iron and Carbon Steels in Air or Oxygen," *Oxidation of Metals*, vol. 59, no. 1, pp. 433–468, 2003.

[57] L. Pinder, K. Dawson, G. Tatlock, and F. Mahi, *High Temperature Corrosion of Low Alloy Steels*. Elsevier Ltd., 2017, no. February 2016. [Online]. Available: http://dx.doi.org/10.1016/B978-0-12-803581-8.01582-4

[58] R. Kornell and U. Schwertmann, *The iron oxides - Structure, Properties, Reactions, Occurences and Uses*. Wiley-VCH Verlag GmbH & Co. KGaA, 2003.

[59] A. Khanna, *Introduction to High Temperature oxidation and corrosion*. ASM International, 2002.

[60] G. C. Wood, "High-temperature oxidation of alloys," *Oxidation of Metals*, vol. 2, no. 1, pp. 11–57, 1970.

[61] W. Bragg, "The structure of the spinel group of crystals ," *The London, Edinburgh, and Dublin Philosophical Magazine and Journal of Science*, vol. 30, no. 176, pp. 305–315, 1915.

[62] A. Zahs, M. Spiegel, and H. J. Grabke, "Chloridation and oxidation of iron, chromium, nickel and their alloys in chloridizing and oxidizing atmospheres at 400-700 degrees C," *Corrosion Science*, vol. 42, no. 6, pp. 1093–1122, 2000.

[63] Y. S. Li, Y. Niu, and W. T. Wu, "Accelerated corrosion of pure Fe, Ni, Cr and several Fe-based alloys induced by $ZnCl_2$-KCl at 450 °C in oxidizing environment," *Materials Science and Engineering*, vol. A345, pp. 64–71, 2003.

[64] F. Wang and Y. Shu, "Influence of Cr content on the corrosion of Fe-Cr alloys: The synergistic effect of NaCl and water vapor," *Oxidation of Metals*, vol. 59, no. 3-4, pp. 201–214, 2003.

[65] S. C. Cha and M. Spiegel, "Local reactions of KCl particles with iron, nickel and chromium surfaces," *Materials and Corrosion*, vol. 57, no. 2, pp. 159–164, 2006.

[66] H. T. Ma, C. H. Zhou, and L. Wang, "High temperature corrosion of pure Fe, Cr and Fe-Cr binary alloys in O_2 containing trace KCl vapour at 750 °C," *Corrosion Science*, vol. 51, no. 8, pp. 1861–1867, 2009.

[67] H. J. Grabke, E. Reese, and M. Spiegel, "The Effects of Chlorides, Hydrogen-Chloride, and Sulfur-Dioxide in the Oxidation of Steels Below Deposits," *Corrosion Science*, vol. 37, no. 7, pp. 1023–1043, 1995.

[68] A. Zahs, M. Spiegel, and H. J. Grabke, "The influence of alloying elements on the chlorine-induced high temperature corrosion of Fe-Cr alloys in oxidizing atmospheres," *Materials and Corrosion*, vol. 50, no. 10, pp. 561–578, 1999.

[69] M. A. Uusitalo, P. M. J. Vuoristo, and T. A. Mantyla, "High temperature corrosion of coatings and boiler steels in oxidizing chlorine-containing atmosphere," *Materials Science and Engineering a-Structural Materials Properties Microstructure and Processing*, vol. 346, no. 1-2, pp. 168–177, 2003.

[70] ——, "High temperature corrosion of coatings and boiler steels below chlorine-containing salt deposits," *Corrosion Science*, vol. 46, no. 6, pp. 1311–1331, 2004.

[71] J. Pettersson, H. Asteman, J. E. Svensson, and L. G. Johansson, "KCl induced corrosion of a 304-type austenitic stainless steel at 600 °C; The role of potassium," *Oxidation of Metals*, vol. 64, no. 1-2, pp. 23–41, 2005.

[72] S. Sroda and S. Tuurna, "Laboratory scale tests on corrosion behavior of boiler materials in simulated combustion atmospheres (EU Project - OPTICORR)," *Materials and Corrosion*, vol. 57, no. 3, pp. 244–251, 2006.

[73] N. Folkeson, L. G. Johansson, and J. E. Svensson, "Initial stages of the HCl-induced high-temperature corrosion of alloy 310," *Journal of the Electrochemical Society*, vol. 154, no. 9, pp. C515–C521, 2007.

[74] C. Pettersson, L. G. Johansson, and J. E. Svensson, "The Influence of Small Amounts of KCl(s) on the Initial Stages of the Corrosion of Alloy Sanicro 28 at 600 °C," *Oxidation of Metals*, vol. 70, no. 5-6, pp. 241–256, 2008.

[75] C. Proff, T. Jonsson, C. Pettersson, J. E. Svensson, L. G. Johansson, and M. Halvarsson, "Microstructural investigation of the KCl-induced corrosion of the austenitic alloy Sanicro 28 (35Fe27Cr31Ni) at 600 °C," *Materials at High Temperatures*, vol. 26, no. 2, pp. 113–125, 2009.

[76] J. Sui, J. Lehmusto, M. Bergelin, and H. Mikko, "The Effects of KCl, NaCl and K_2CO_3 on the High-Temperature Oxidation Onset of Sanicro 28 Steel," *Oxidation of metals*, vol. 85, pp. 565–598, 2016.

[77] D. Bramhoff, H. J. Grabke, E. Reese, and H. P. Schmidt, "Einfluß von HCl und Cl_2 auf die Hochtemperaturkorrosion des 2 1/4 Cr 1 Mo-Stahls in Atmosphären mit hohen Sauerstoffdrücken," *Materials and Corrosion*, vol. 41, no. 6, pp. 303–307, 1990.

[78] E. Reese and H. J. Grabke, "Einflun von Chloriden auf die Oxidation," *Werkstoffe und Korrosion*, vol. 43, pp. 547–557, 1992.

[79] S. Środa, S. Tuurna, K. Penttilä, and L. Heikinheimo, "High Temperature Oxidation Behaviour of Boiler Steels under Simulated Combustion Gases," *Materials Science Forum*, vol. 461-464, pp. 981–988, 2004.

[80] N. Folkeson, T. Jonsson, M. Halvarsson, L. G. Johansson, and J. E. Svensson, "The influence of small amounts of KCl(s) on the high temperature corrosion of a Fe-2.25Cr-1Mo steel at 400 and 500 °C," *Materials and Corrosion*, vol. 62, no. 7, pp. 606–615, 2011.

[81] T. Jonsson, N. Folkeson, J.-E. Svensson, L.-G. Johansson, and M. Halvarsson, "An ESEM in situ investigation of initial stages of the KCl induced high temperature corrosion of a Fe–2.25Cr–1Mo steel at 400 °C," *Corrosion science*, vol. 53, pp. 2233–2246, 2011.

[82] A. M. Olivas Ogaz, J. Eklund, A. Persdotter, M. Sattari, J. Liske, J.-E. Svensson, and T. Jonsson, "The Influence of Oxide-Scale Microstructure on KCl(s)-Induced Corrosion of Low-Alloyed Steel at 400 °C," *Oxidation of Metals*, vol. 91, no. 3-4, pp. 291–310, 2019.

[83] E. Larsson, J. Liske, A. Persdotter, T. Jonsson, J. E. Svensson, and L. G. Johansson, "The Influence of KCl and HCl on the High-Temperature Oxidation of a Fe-2.25Cr-1Mo Steel at 400 °C," *Oxidation of Metals*, vol. 93, no. 1-2, pp. 29–52, 2020.

[84] S. Reyntjens and R. Puers, "A review of focused ion beam applications in microsystem technology," *Journal of micromechanics and microengineering 11*, p. 287–300, 2001.

[85] J.Goldstein, D. Newbury, D. Joy, C. Lyman, P. Echlin, E. Lifshin, L. Sawyer, and J. Michael, "Scanning Electron Microscopy and X-ray Microanalysis," *(Third edition)*, 2007.

[86] D. B. Williams and C. B. Carter, *Transmission electron microscopy, A textbook for materials science.* New York: Springer Science + Business Media, 2009.

[87] J. Orloff, M. Utlaut, and L. Swanson, *High Resolution Focused Ion Beams: FIB and its Applications.* New York: Kluwer academic/Plenum publishers, 2003.

[88] D. C. Cox, "Introduction to Focused Ion Beam Nanometrology," *Morgan and Claypool Publishers*, 2015.

[89] B. Gault, M. P. Moody, J. M. Cairney, and S. P. Ringer, *Experimental Protocols in Atom Probe Tomography*. Springer Science+Business Media,, 2012, vol. 160.

[90] B. D. Cullity, *Elements of X-ray diffraction*. Pearson Education, 2014.

[91] R. A. Schwarzer, D. P. Field, B. L. Adams, M. Kumar, and A. J. Schwartz, *Present State of Electron Backscatter Diffraction and Prospective Developments*. Boston, MA: Springer US, 2009, pp. 1–20.

[92] B. Pujilaksono, T. Jonsson, M. Halvarsson, J. E. Svensson, and L. G. Johansson, "Oxidation of iron at 400-600 °C in dry and wet O_2," *Corrosion Science*, vol. 52, no. 5, pp. 1560–1569, 2010.

[93] A. N. Hansson, M. Montgomery, and M. A. Somers, "Development of the inner oxide zone upon steam oxidation of an austenitic stainless steel," *Materials at High Temperatures*, vol. 26, no. 1, pp. 39–44, 2009.

[94] J.-O. Andersson, T. Helander, L. Höglund, P. Shi, and B. Sundman, "THERMO-CALC & DICTRA, Computational Tools For Materials Science," *Calphad*, vol. 26, no. 2, pp. 273–312, 2002.

[95] V. Ssenteza, J. Eklund, S. Bigdeli, and T. Jonsson, "Long-term corrosion behavior of FeCr(Al, Ni) alloys in O_2 + H_2O with KCl(s) at 600 °C: Microstructural evolution after breakaway oxidation," *Unpublished*, 2023.

[96] J. Pettersson, J. E. Svensson, and L. G. Johansson, "Alkali Induced Corrosion of 304-type Austenitic Stainless Steel at 600 °C; Comparison between KCl, K_2CO_3 and K_2SO_4," *Materials Science Forum*, vol. 595-598, pp. 367–375, 2008.

[97] T. Jonsson, B. Pujilaksono, A. Fuchs, J.-E. Svensson, L. G. Johansson, and M. Halvarsson, "The influence of h_2o on iron oxidation at 600 °c: A microstructural study," in *High Temperature Corrosion and Protection of Materials 7*, ser. Materials Science Forum, vol. 595. Trans Tech Publications Ltd, 12 2008, pp. 1005–1012.

[98] W. Freer and R. O'Reilly, " The diffusion of Fe 2+ ions in spinels with relevance to the process of maghemitization ," *Mineralogical Magazine*, vol. 43, no. 331, pp. 889–899, 1980.